

Finite-friction least-thickness self-standing domains of symmetric circular masonry arches

Giuseppe COCCHETTI^{1,2}, Egidio RIZZI^{2,*}

¹Politecnico di Milano, Dipartimento di Ingegneria Civile e Ambientale,
piazza Leonardo da Vinci 32, I-20133 MILANO, Italy

²Università degli studi di Bergamo, Dipartimento di Ingegneria e Scienze Applicate,
viale Guglielmo Marconi 5, I-24044 DALMINE (BG), Italy

*Corresponding Author: egidio.rizzi@unibg.it

Accepted Preprint: 19 June 2024

Abstract

This paper concerns a general aspect, in the mechanics of masonry arches, with reference to symmetric circular geometries, with variable opening, and possible stereotomy with radial joints (to be potentially formed, at failure, within an ideal continuous arch), in a limit least-thickness condition, under self-weight, namely the role that a finite inherent (Coulomb) friction, among the theoretical joints, may play in ruling the self-standing conditions and the mechanical features at incipient collapse, setting a change from purely-rotational modes to mechanisms that may include sliding. The matter is first systematically investigated, by a full analytical treatment, then validated and illustrated through an original Complementarity Problem/Mathematical Programming formulation, and numerical implementation, reconstructing the complete underlying map of thickness-to-radius ratio versus friction coefficient of all arch states, and corresponding collapse mechanisms and relevant characteristic features. This investigation shall clear the issue, of the theoretical influence of finite friction, in the above-stated setting, and contribute to provide a full understanding of fundamental aspects in the methodological description, and physical interpretation, of the mechanics of masonry arches, in terms of natural bearing capacity, as linked to structural form optimization and relying on basic underlying physical properties such as a finite amount of inherent friction, with implications that may come up to appear also in practical terms, once dealing with this traditional and remarkable structures, in real cases, possibly endowed of a historical character and architectural value, to be currently preserved and renewed.

Keywords: (*symmetric circular*) *masonry arches*; *Couplet-Heyman problem*; *least thickness*; *collapse modes*; *finite friction*.

1 Introduction

The self-standing (symmetric circular) continuous masonry arch (with ideal stereotomy displaying radial joints) of least thickness constitutes a fascinating example of structural form optimization (“Couplet-Heyman problem”), which may even be appreciated in related beautiful natural manifestations that likely shall have inspired ancient builders in conceiving and devel-

oping this classical form of bearing structure, through, first, empirical rules of construction and, then, sedimented attempts in mechanical codifications.

In “modern” times, this has been investigated on a rational basis within the Mechanics of masonry structures, which has settled over the last few centuries, specifically since 1700, after the contributions by Pierre Couplet, coming, since the beginning of 1900, to contemporary thrust-line analyses, from cornerstone Milutin Milankovitch formulation [1–3] and, in the second half of 1900, to the codifications in the realm of Limit Analysis of masonry constructions, according to the much recent light-breaking studies by Jacques Heyman [4–9]. The latter were based on three classical behavioural assumptions for typical masonry constructions: (I) no tensile strength; (II) infinite compressive strength; (III) no sliding failure. Specifically, the last stated hypothesis shall rule out the possible onset of sliding manifestations within the masonry arch, as e.g. per the presence of a high or even infinite amount of inherent friction, and allows to characterize the main failure mechanisms of the masonry arch related just to purely-rotational collapse.

That has widely been adopted to elucidate the statics of continuous and discrete (symmetric circular) masonry arches under self-weight, at variable half-opening angle α , with remarkable and fundamental results in terms of kinematical (e.g. angular intrados inner-hinge position from the crown $\beta = \beta_r$, of the resulting symmetric five-hinge purely-rotational collapse mode), geometrical (e.g. thickness-to-radius ratio $\eta = t/r$) and statical (e.g. non-dimensional horizontal thrust $h = H/[(\gamma td) r]$ or alternatively intrinsic non-dimensional horizontal thrust $\hat{h} = \eta h = H/(\gamma dr^2)$ at given arch characteristics: γ uniform specific self-weight per unit volume; d out-of-plane depth; r mean radius) arch features at incipient collapse, in the critical least-thickness self-standing condition.

The whole has originally been revisited and cleared through a comprehensive mechanical analysis by the present authors [10–15], where focus was first made on a complete analytical derivation, with separate numerical validations, of the conditions of purely-rotational collapse [10, 11, 14, 15]. Then, on the investigation of the manifestation of possible sliding, friction effects have initially been investigated, in order to inspect the presence of potential sliding failure at reducing friction, namely as linked to a finite Coulomb friction coefficient [12, 13]. This has first analytically been revealed for the complete semi-circular arch ($\alpha = \pi/2$) [12], where all basic underlying equations were derived, and explored, for such a specific case, with initial perspectives in terms of additional implications at variable half-angle of embrace of the arch, as further numerically investigated in [13], whereby an original Complementarity Problem/Mathematical Programming (CP/MP) numerical formulation and self-implementation was also developed and run to the purpose. The latter has also been adopted to systematically illustrate statical and kinematical features of both purely-rotational collapse modes [14], and indeed collapse mechanisms involving sliding [13], while independent numerical validations by an available Discontinuous Deformation Analysis (DDA) modelization, as pertinent to a Discrete Element Method (DEM) approach [11, 14], and by a simple self-assembled numerical optimization sheet solver [12], have also separately been provided, as a form of parallel corroborating numerical experimentation.

Such personal efforts have been framed within a rather flourishing external literature dedicated to the specific subject, where least-thickness conditions of masonry arches have been enquired by different analytical-numerical approaches, aimed at revealing the above-mentioned characteristic features [16–45], and by modern thrust-line analyses, following cornerstone Mi-

lankovitch formulation [1–3], particularly in view of achieving masonry arch form optimization [46–53]. Specifically, as per the characterization of purely-rotational collapse, these works have constituted a basic and complementary information concerning the aforesaid issues, while, as per the specific investigation on finite-friction effects, works [54–69], with already mentioned [20, 42–45] and [39], have separately provided a quite solid basis and reference framework, to be complemented, still, by additional, systematic treatments, to be analytically pursued, whenever possible, as herein primarily sought.

The present paper systematically addresses the issue of reducing friction (interpreted through a standard Coulomb friction law), at general half-opening angle α of the symmetric circular masonry arch from the crown, by outlining all characteristic features and locating all possible collapse modes that may be manifested. This is developed by a comprehensive analytical approach, where all governing (equilibrium and limit compatibility) equations are derived, and resolved until a very end. All self-standing states of the arch are characterized and separated by the arising collapse modes, in the critical least-thickness/finite-friction condition, by revealing rather interesting and multi-fold features of such an ideally simple mechanical system. Indeed, and instead, the appearance of even a single, new system parameter (Coulomb masonry friction angle φ or friction coefficient $\mu = \tan \varphi$) brings in surprising manifestations, in all sought admissible ranges of the physical parameters. The analytically derived states of the masonry arch are then further illustrated through the above-mentioned CP/MP numerical formulation [13], which is also here meant to supply, at the same time, a sort of independent/interrelated numerical experimental validation of the previous rigorous analytical treatment.

Current reference is here made just to the ideal classical Heyman-like uniform self-weight distribution along the geometrical centreline of the circular arch [4–8], although truly referring to the correct least-thickness solution [9], as widely analytically outlined and discussed in [10, 11, 14, 15], for the (symmetric) purely-rotational collapse mode. Thereby, the analysis was contextually developed also for the true Milankovitch-like uniform self-weight distribution [1–3], accounting for the real centres of gravity of the ideal chunks of the arch, which leads to a generalized, though little more complicated, case of mechanical analysis, by developing a complete comparison among Heyman (“*1st-order algebraic problem*”), current correct (“*2nd-order algebraic problem*”) and Milankovitch (“*3rd-order algebraic problem*”) solutions [10, 15]. Thus, at the entrance of finite (Coulomb) friction, into the mechanical scene, as an additional relevant physical parameter of the system, the analysis is here developed, by now, only for the classical Heyman-like self-weight distribution, given the contained differences experienced for the purely-rotational collapse states at infinite friction, though the further extension to a Milankovitch-like self-weight treatment shall be possible, in principle, as a generalization of the present analysis, and recorded outcomes.

Presentation flows as follows. Subsequent Section 2 outlines the basic underlying mechanical equations ruling the present analytical treatment. Section 3 delivers the main body of the proposed analytical outcomes, by reporting the various solution instances of the governing equations, and illustrating them, based on the variable physical parameters that come into place. Section 4 portrays the various arch states at incipient collapse, through a separate running of a CP/MP numerical formulation, providing a corresponding, though independent, numerical validation. Finally, closing Section 5 gathers the main aspects and achievements of the study and traces down some further research perspectives, in terms of possible generalizations of the present endeavours to other masonry arch features.

2 Underlying relations and analytical treatment

The underlying governing equations of the Mechanics of (symmetric circular) continuous masonry arches rely on the (correct) Heyman-like treatment of purely-rotational collapse [6, 9, 10] and on the introduction of the account of finite friction [12]. Assuming the (symmetric) purely-rotational collapse mode (at an infinite or finite supercritical friction) as given from scratch, critical arch characteristics in the least-thickness condition $\beta = \beta_r, \eta, h$ can be determined (Figs. 1–2), by equilibrium and (least-thickness) optimality (intrados tangency of the line of thrust, as locus of pressure points along the arch) conditions [10, 14, 15].

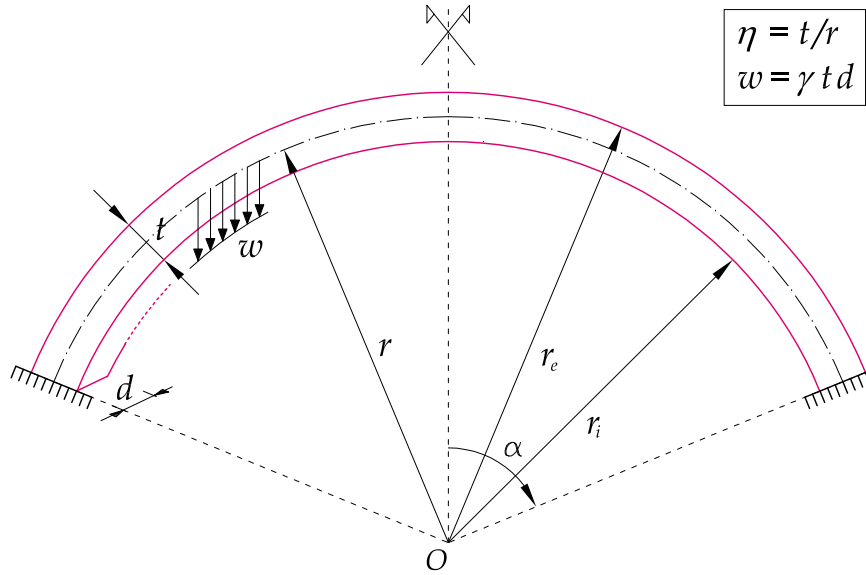


Figure 1: Symmetric circular masonry arch under self-weight (γ specific weight per unit volume) with involved characteristic parameters (d out-of-plane depth).

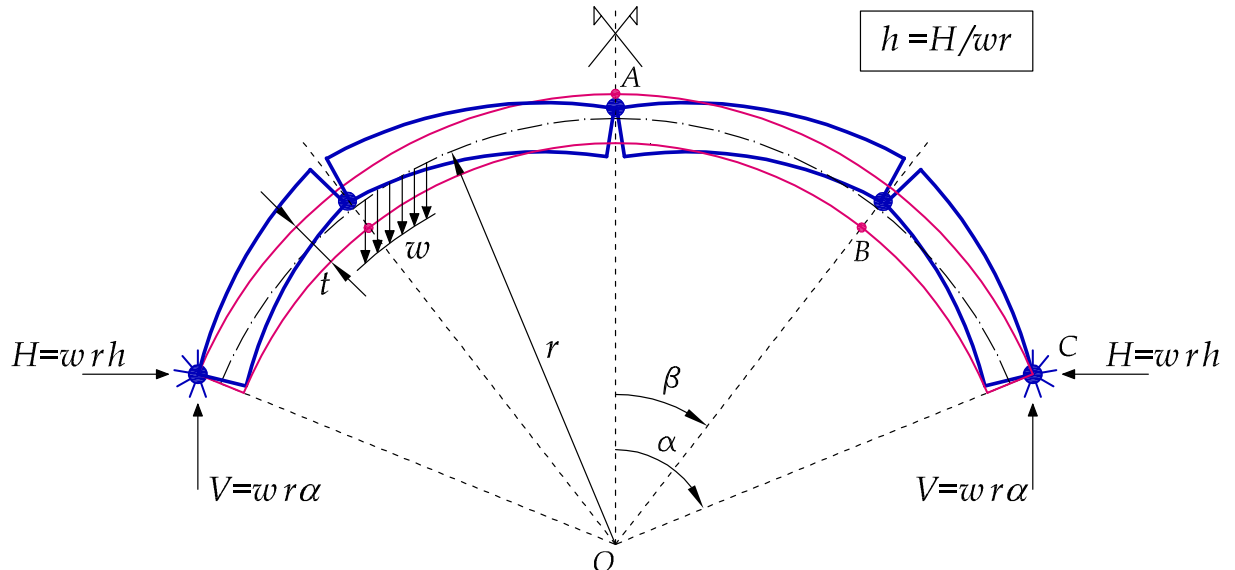


Figure 2: Least-thickness “Couplet-Heyman problem”. Purely-rotational collapse mode, with shoulder-hinge reactions V and H (opposite of weight of half-arch and horizontal thrust). Characteristic variables: angular inner-hinge position $\beta = \beta_r$, thickness-to-radius ratio $\eta = t/r$ and non-dimensional horizontal thrust $h = H/(wr)$.

At reducing friction, the appearance of joint sliding is ruled by additional equations [12], which sets in a hierarchy of the various collapse modes that can be recorded, at variable half-angle of embrace α of the circular masonry arch, and its inherent friction coefficient $\mu = \tan \varphi$. Thus, a first approach relies on the assumed purely-rotational collapse mode, and attached discovered analytical solutions, and foresees new potential (sliding) occurrences based on the value of a reducing (finite) friction coefficient.

Then, the mechanical problem is governed by the fundamental underlying equations described as follows, see [10, 14, 15] and [12], with notation and meaning therein set.

For the characterization of purely-rotational collapse, at a high or infinite friction coefficient [10, 14, 15]:

- equilibrium relation concerning the relative rotational equilibrium of any upper or lower portion of the half-arch (symmetry conditions apply), with respect to the inner intrados hinge forming at the haunch at angular position $\beta = \beta_r$ from the crown ($h_1 = h_L$ “Lower thrust”, h_U “Upper thrust”, see [17] and [14]):

$$h = h_1 = h_L(\beta, \eta) = \frac{(2 - \eta)\beta \sin \beta - 2(1 - \cos \beta)}{2 + \eta - (2 - \eta)\cos \beta} \quad (1)$$

or

$$h = h_U(\alpha, \beta, \eta) = \frac{(2 + \eta)\alpha \sin \alpha - (2 - \eta)\beta \sin \beta - 2(\cos \beta - \cos \alpha)}{(2 - \eta)\cos \beta - (2 + \eta)\cos \alpha} \quad (2)$$

- equilibrium relation concerning the absolute rotational equilibrium of the whole half-arch, with respect to the extrados hinge at the shoulder, involving a dependence on half-opening angle α , just through variable $A(\alpha) = \alpha \cot(\alpha/2)$:

$$h = h_2(\alpha, \eta) = A(\alpha) - \frac{2}{2 + \eta}, \quad A(\alpha) = \frac{\alpha \sin \alpha}{1 - \cos \alpha} = \alpha \cot \frac{\alpha}{2} \quad (3)$$

- limit (truly correct) tangency condition of the line of thrust (locus of pressure points) at the haunch intrados in the least-thickness condition (updated from single term h_H characteristic of “approximate” Heyman solution with η small), which can be expressed by a stationary condition:

$$h = h_e(\beta, \eta) = \underbrace{\beta \cot \beta}_{h_H} - \frac{\eta}{2 - \eta} \quad (4)$$

The corresponding (correct) **purely-rotational solution** can be derived in explicit analytical form, out of the following “quadratic algebraic problem” in triplet $A(\beta)$, $\eta(\beta)$, $h(\beta)$ [10, 15]:

$$\begin{cases} pol_A = S(2g - S)A^2 - 2fgA + g^2 = 0 \\ pol_\eta = (f + g)\eta^2 - 4(g - S)\eta + 4(g - f) = 0 \\ pol_h = 2S h^2 - 2(f - S)h + g - f = 0 \end{cases} \quad (5)$$

where

$$\begin{aligned} f &= (\beta S)' = S + \beta C, & g &= fC + \beta S^2 = \beta + SC; \\ S &= \sin \beta, \quad C = \cos \beta; & \text{with link } \beta S^2 + Cf - g = 0 \end{aligned} \tag{6}$$

and symbol ' denotes first-order differentiation with respect to angular position β .

The arising purely-rotational solution can be obtained by the two-branched explicit analytical solution of second-order Eqs. (5), as follows:

$$\begin{aligned} A &= g \frac{f \pm \sqrt{f^2 - 2gS + S^2}}{S(2g - S)} \\ \eta &= 2 \frac{g - S \mp \sqrt{f^2 - 2gS + S^2}}{f + g} \\ h &= \frac{f - S \pm \sqrt{f^2 - 2gS + S^2}}{2S} \end{aligned} \tag{7}$$

where term $f^2 - 2gS + S^2$ under square root vanishes for $\beta_{s\beta} = 1.129085087576187 \simeq 64.7^\circ$ [10], representing the widest angular inner-hinge position for the purely-rotational collapse mode (at $\alpha = \alpha_{s\beta} = 2.230312828619947 \simeq 127.8^\circ$) [15], separating the two-valued branches of the purely-rotational solution at variable β .

The achieved explicit two-branched purely-rotational solution (in terms of variable A) is reported in the analytical-numerical plots depicted in Fig. 3, for classical Heyman triplet β, η, h [10, 14, 15], as a function of α , whereby a numerical root finding is needed just to resolve transcendental equation $A(\alpha) = \alpha \cot(\alpha/2)$, to finally express the sought dependence on source half-opening angle α .

Such a purely-rotational solution holds true until $\alpha = \alpha_l = 2.648388899151005 \simeq 151.7^\circ$, where $\beta = \beta_r$ pulls back to 0, while η and h reach the rather peculiar values of $\eta = 1$ ($t = r$) and $h = 0$, representing a shift to a purely-overturning mode, of each half-arch, with respect to the extrados hinge at the shoulder, with line of action of half-arch weight exactly aligned onto it, as further discussed next, in the context of finite/infinite friction.

Notice that, while being two-valued, the solution branches turn out monotonic for the main global arch characteristics, i.e. η and h , as per classical Heyman solution (and interestingly stay rather near to that, confirming the validity of such a pioneering solution), while they turn out non-monotonic, for inner-hinge variable $\beta = \beta_r$, as an internal ingredient of arch collapse appearance and as a main difference to “approximate” Heyman solution, basically holding for η small, thus, say, for up-to-complete circular arches, with visible growing differences, on $\beta = \beta_r$, for over-complete arches, at increasing half-opening angle α .

All these aspects, with a comprehensive comparison also to a Milankovitch-like solution, with a true uniform self-weight distribution, have extensively been illustrated and described in previous works [10, 14, 15], by full analytical explicit representations (including for the roots of cubic Milankovitch problem, similar to Eqs. (7), in last paper [15], from which the interested reader may now start with, to consult the various purely-rotational solutions, and also appreciate peculiar revealed analytical features such as the maximum intrinsic non-dimensional horizontal thrust \hat{h} reachable within the circular masonry arch).

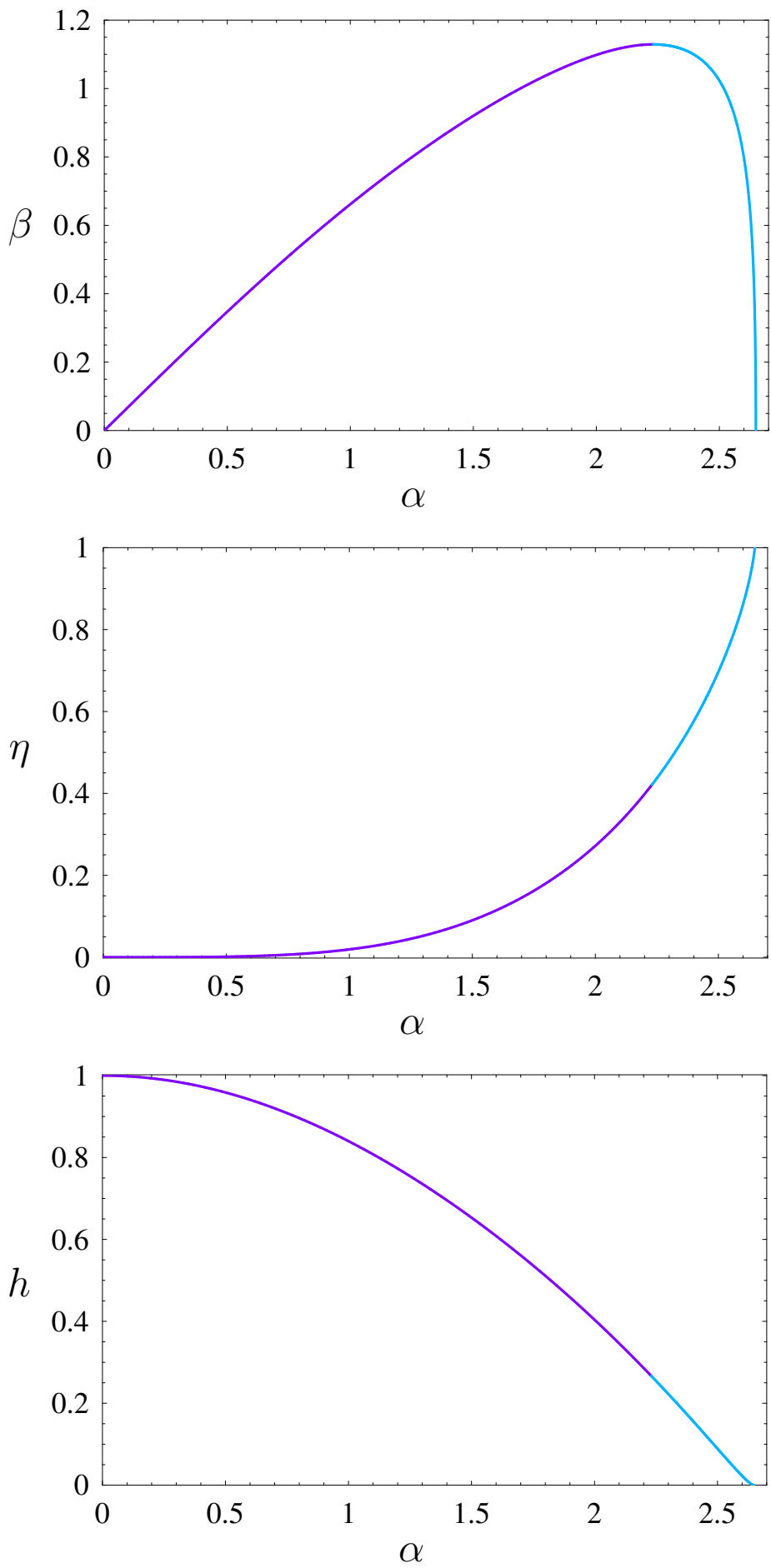


Figure 3: Purely-rotational least-thickness solution for triplet $\beta = \beta_r, \eta, h$ as a function of α .

For the characterization of sliding onset, at a finite reducing friction coefficient [12]:

- sliding relation setting the activation of a shoulder sliding joint:

$$\mu = \mu_{ss}(\alpha, h) = \frac{h \sin \alpha - \alpha \cos \alpha}{h \cos \alpha + \alpha \sin \alpha} \quad \text{or} \quad h = h_\mu(\alpha, \mu) = \alpha \frac{\cos \alpha + \mu \sin \alpha}{\sin \alpha - \mu \cos \alpha} \quad (8)$$

- sliding relation setting the activation of an inner sliding joint, in the least-thickness condition, which can be expressed by a stationary condition, at angular location $\beta = \beta_s$:

$$\mu = \mu_{is}(h) = \left. \frac{(1-h) \cos \beta - \beta \sin \beta}{(1-h) \sin \beta + \beta \cos \beta} \right|_{\beta = \beta_s(h)} = \sqrt{h(1-h)} \quad (9)$$

The resultancies of Eq. (9), for **inner sliding joint activation**, are graphically depicted in Fig. 4, as a function of friction coefficient μ , in showing resulting dependencies $h(\mu)$ and $\beta_s(\mu)$, as controlled by the amount of inherent friction within the masonry arch.

Remark: Notice that, at a sliding activation, finite friction coefficient μ sets the value of horizontal thrust h within the masonry arch.

Despite, the notation adopted in Eqs. (8)-(9) much easily represents the dependencies in terms of friction coefficient $\mu = \mu(h)$, for both equations, instead as in terms of thrust $h = h(\mu)$, as it was earlier employed in Eqs. (1)-(4), which, only for Eq. (8), could also explicitly be expressed as $h = h_\mu = \alpha(\cos \alpha + \mu \sin \alpha)/(\sin \alpha - \mu \cos \alpha)$ [12]. Moreover, notice that no dependence on thickness-to-radius ratio η is seen, in the sliding activation equations, similarly as for friction coefficient μ , in purely-rotational Eqs. (1)-(4), while sliding dependence on half-opening angle α is brought about just by shoulder sliding activation Eq. (8).

Once both Eqs. (8)-(9) hold, a **purely-sliding collapse mode** is set, within the masonry arch, which may here be represented by solution triplet $\beta = \beta_s$, μ , h as a function of α , somehow resembling the earlier purely-rotational representation of $\beta = \beta_r$, η , h in Fig. 3, as further depicted in Fig. 5 (red lines). Here, notice that friction coefficient μ is taken, in the mid of Fig. 5, instead of thickness-to-radius ratio η , in the mid of Fig. 3, being η undefined in the purely-sliding equations, to now describe, instead, the correspondence between μ and α , within the manifestation of purely-sliding collapse modes. Thus, once α or μ is set, μ or α is found, and h accordingly, with resulting angular position of the inner sliding joint as $\beta = \beta_s(h) = \sqrt{h(1-h)}$.

Notice that, in the lower plot of $h(\alpha)$ in Fig. 5, the branch of the purely-rotational solution from the lower plot of $h(\alpha)$ in Fig. 3 is as well reported, to highlight the presence of an intersection point coming to arise between the two lines, occurring for $\alpha_T = 2.487161163767182 \simeq 142.5^\circ$, at $h = 0.09780581933963814$, leading to $\beta_s = 0.2970519164101457$ and $\mu = 1.415270827756886$, for the purely-sliding solution, and to $\beta_r = 1.037485213550072$ and $\eta = 0.6796047320988860$, for the purely-rotational solution, marking a joining link, and direct shift, between purely-rotational and purely-sliding solution, as it will characteristically be discussed in the sequel.

Moreover, the plots of the purely-sliding solution in Fig. 5 shall in principle be reported for a half-opening angle α varying from 0 to π . However, as connected to the value of critical thickness, with non-apparent role in Eqs. (8)-(9), it will be seen that the practical α range for the purely-sliding mode shall be limited from above by the upper value of $\alpha_B = 2.774176793356034 \simeq 159^\circ$, corresponding to limit mark $\eta = 2$ ($t = 2r$), at $\mu = 2.690297881776621$ ($\varphi \simeq 70^\circ$), as it will also be discussed in the next sections. Thus, (red) lines in Fig. 5 become dashed, after that α value.

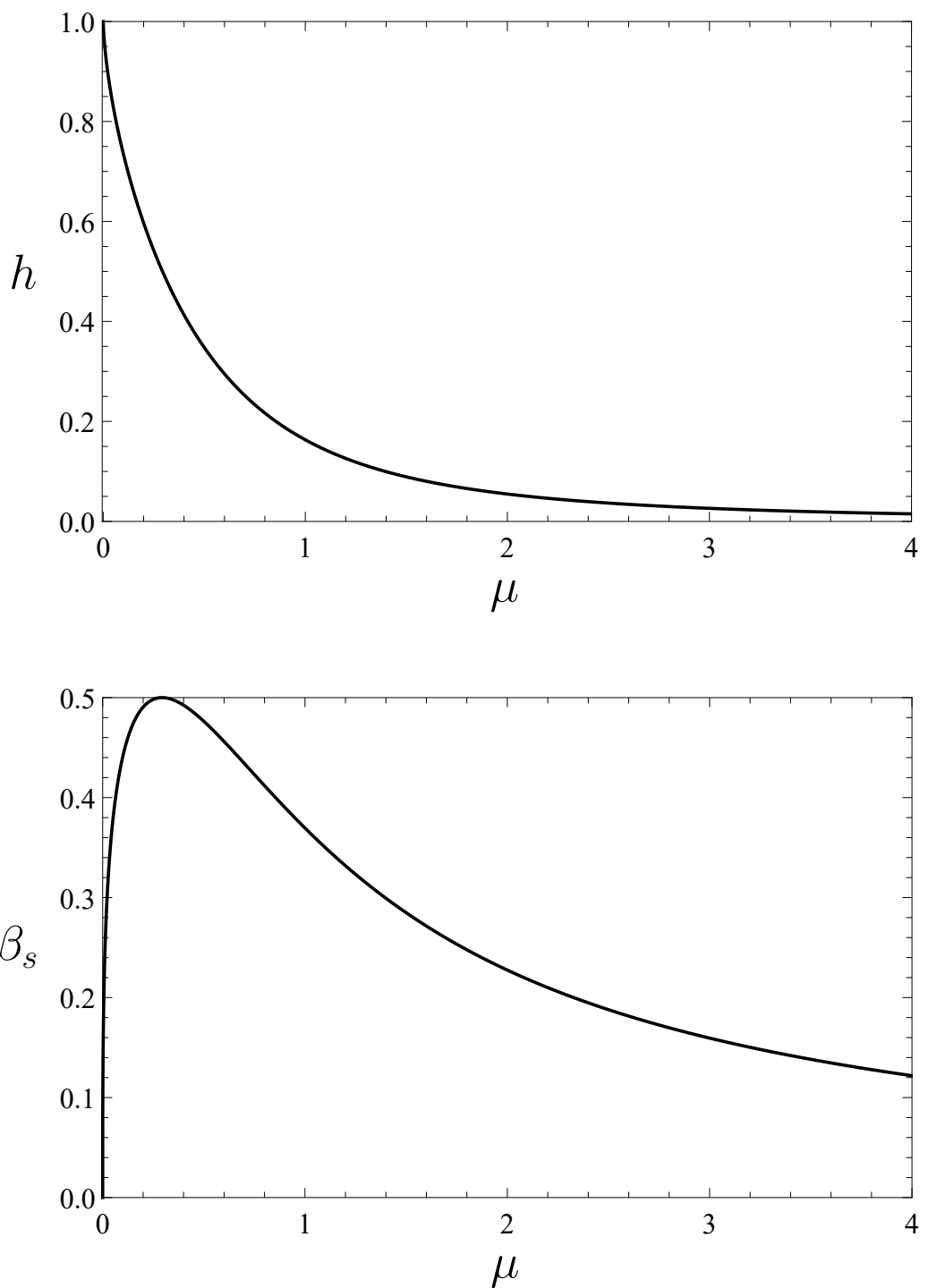


Figure 4: Relations h of μ (top) and β_s of μ (low) at inner sliding activation.

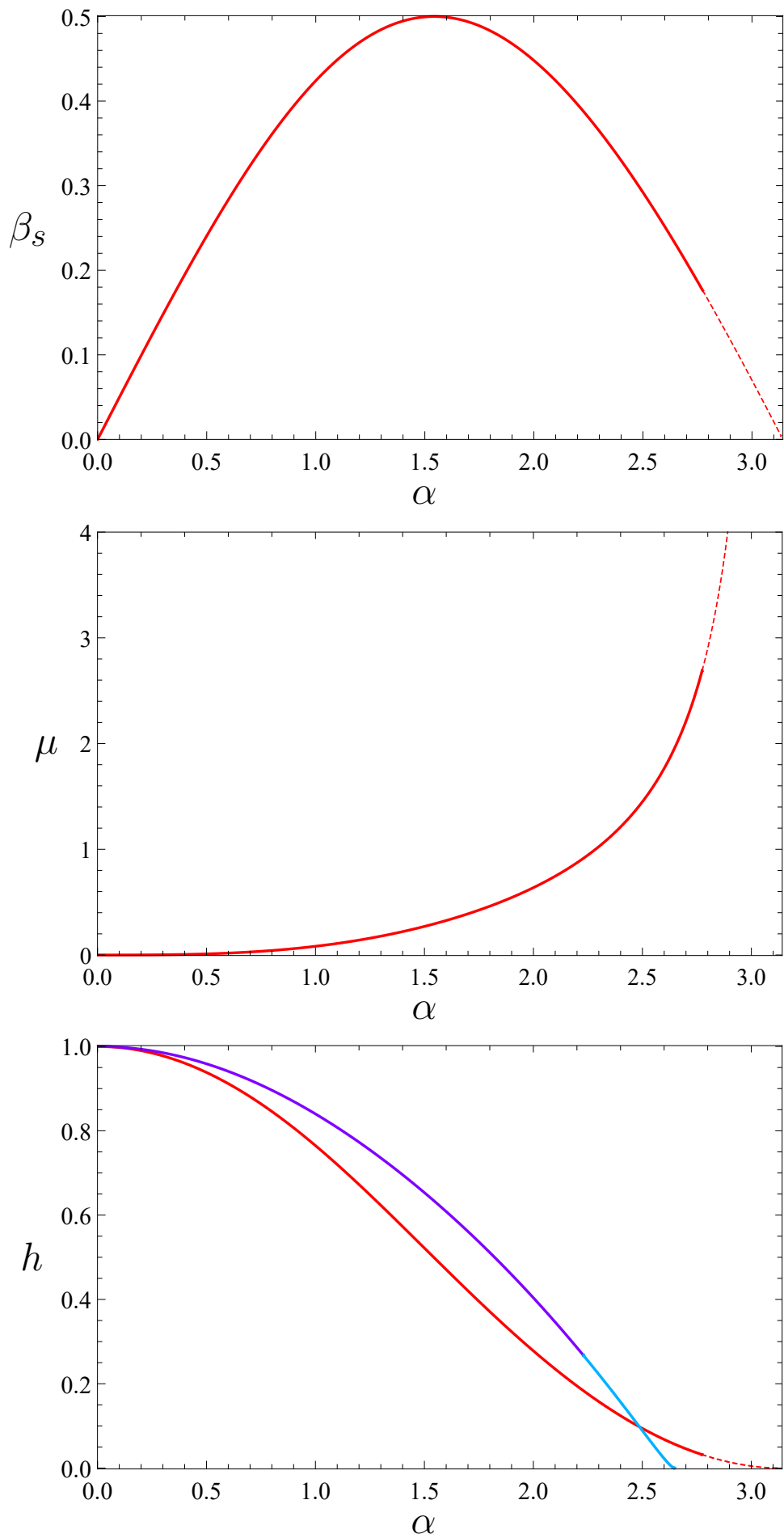


Figure 5: Purely-sliding solution for triplet $\beta = \beta_s, \mu, h$ as a function of α .

Resuming, the first group of three underlying equations, Eqs. (1)-(4), describes by itself the least-thickness condition for the purely-rotational collapse mode, as classically set by Heyman analysis, but with a true imposition of the tangency of the line of thrust at the intrados of the arch [6, 9, 10]; the second group of two sliding relations, Eqs. (8)-(9), considers the possible activation of sliding joints, at the arch shoulder or/and at an inner sliding joint [12], and describes by itself the purely-sliding collapse mode. Once part of the three purely-rotational equations and of the two sliding relations are active, mixed collapse mechanisms involving rotation/sliding may arise. The mechanical system is then ruled, in general, by 5 governing equations in terms of 5 variables, α , μ and η , h , $\beta = \beta_r$, while $\beta = \beta_s$ is implicitly represented as $\beta_s = \sqrt{h(1-h)}$.

Then, the interplay of the above governing relations allows to derive a full map of the various manifestations of the considered mechanical system, in terms of admissible self-standing domains and collapse states, and separating boundaries between them. Primarily, a thickness-to-radius ratio vs. friction coefficient $\eta\text{-}\mu$ two-dimensional projection diagram of the system (at implicitly variable half-opening angle α) can be derived, and depicted, with the representation of all admissible masonry arch states and collapse types, as illustrated in Section 3. Before that, additional complementary analytical considerations may be in order.

2.1 Additional analytical interpretations

At such a stage, a further, complete analytical treatment may additionally be developed, disregarding the role of any pre-assumed purely-rotational (Heyman-like) mechanism at infinite friction, to start with, as a leading benchmark reference and guideline, in the mechanical analysis. Indeed, the previous derivation looks exhaustive by itself but comes from the initial assumption of an underlying (correct) Heyman-like purely-rotational condition, by further inspecting, then, the possible insertion and consequence of finite-friction effects. Thus, one may wonder if search may be biased and if anything may be missing within that.

Toward deriving all possible self-standing states of the symmetric circular arch, with no a priori hypotheses on the underlying collapse mode, a subsequent approach may be set by outlining all equilibrium and limit relations, in terms of classical “*line of thrust*” (locus of pressure points, of classical non-dimensional eccentricity $\hat{e} = [M/N]/[t/2] = e/[t/2]$, i.e. moment over axial compression force ratio within the arch, normalized so that to be ± 1 at rotational joint activation [10]), and of original “*line of friction*” (locus of shear over normal force ratio, normalized as $\hat{e}_s = [T/N]/\mu = e_s/[t/2]$, so that to be ± 1 at sliding joint activation [13]). This is further based on the following two groups (as above) of self-coherent main (3 + 2) ruling underlying equations of the (rotational + sliding) physical arch states.

Rotational onset:

- eccentricity of the line of thrust setting the passage from the haunch intrados:

$$\hat{e}(\beta_r) = 1 \quad (10)$$

- eccentricity of the line of thrust setting the passage from the shoulder extrados:

$$\hat{e}(\alpha) = -1 \quad (11)$$

- stationary condition of the eccentricity of the line of thrust at the haunch intrados, as per a line-of-thrust tangency condition there:

$$\hat{e}'(\beta_r)|_{\hat{e}(\beta_r)=1} = 0 \quad (12)$$

Sliding onset:

- eccentricity of the line of friction setting the passage from the shoulder extrados:

$$\hat{e}_s(\alpha) = -1 \quad (13)$$

- stationary condition of the eccentricity of the line of friction at the inner sliding joint intrados, as per a line-of-friction tangency condition there:

$$\hat{e}'_s(\beta_s)|_{\hat{e}_s(\beta_s)=1} = 0 \quad (14)$$

The analytical treatment of either set of 5 system equations, Eqs. (1)-(4) and (8)-(9), or Eqs. (10)-(12) and (13)-(14), leads to the same outcomes, in terms of least-thickness self-standing collapse states and arising characteristic features of the masonry arch configurations. This provides a full, complete demonstration that no further withstanding or collapse states of the arch shall appear, beyond those that spontaneously come up from a classical (though updated) Heyman-like analysis, after the insertion of finite-friction effects, releasing third Heyman hypothesis of no sliding failure.

Actually, to say the truth, in the real chronological developments, a part from this a posteriori resuming presentation, such an analytical way to proceed (with eccentricities) was synergically explored together with the previous one (with direct equations), and also with the parallel support of the CP/MP numerical formulation, later adopted in Section 4, and truly helped in corroborating and providing a main guideline, of treatment and derivation, specifically to locate the self-standing arch states and collapse modes appearing above a “Triple point” revealed in the main η - μ plot presented next, and markedly those for the extended thickness-to-radius ratio $1 \leq \eta \leq 2$ range representing sliding evolutions and manifestations that may be achieved beyond the limit condition of zero horizontal thrust, at $\eta = 1$, for the validity of purely-rotational collapse at infinite friction $\mu \rightarrow \infty$ [10].

With such a complete analytical approach, all self-standing states of the (symmetric circular) masonry arch at variable friction can systematically be outlined. The above presentation sequence aims at reconciling the previous (by now) “classical” derivation, starting from (correct) Heyman-like purely-rotational collapse, and the present one, fully accounting for the presence of finite-friction effects, and revealing all related arising (symmetric) collapse modes, possibly endowed with sliding. All pertinent outcomes are eventually presented next.

3 Self-standing domains and collapse characteristics

After a careful analytical screening of governing mechanical rotational Eqs. (1)-(4) and sliding Eqs. (8)-(9), a main two-dimensional η - μ projection plot (with implicit dependence on α) condensing the results of the various masonry arch states can analytically be drawn (Fig. 6), with

additional zooms for $0 \leq \eta \leq 1$ (Fig. 7) and $0.6 \leq \eta \leq 2$ (Fig. 8), for a wider appreciation. They truly constitute the complete analytical map of the least-thickness solution, endowed with finite-friction effects, with main reported characteristic paths, underlying equations and data, as a main, condensing outcome of the present contribution.

Salient characteristic features that may be deduced by the inspection of the η - μ plot in Fig. 6 (and attached Figs. 7-8) may briefly be discussed as follows:

- The plot analytically reports the main dorsal lines describing joint sliding activations, at finite friction coefficient μ . All depicted lines in the figure are drawn by analytical plots, either driven with explicit functions or by parametric plots, as ruled by the above governing equations. Solid lines mark feasible physical arch states, while dashed lines represent analytical lines that cease to mark valid physical states, though still helping to appreciate the transition and intertwining among them, and the underlying mathematical description by the above-described governing equations.
- The involved equations associated to the main dorsal lines separating the domains of the masonry arch states are directly reported within the plot. Specifically, they mark the conditions of shoulder sliding activation (lines involving $\mu = \mu_{ss}$) or/and inner sliding activation (lines involving $\mu = \mu_{is}$). They come up to intersect at a characteristic “Triple point” ($\eta_T = 0.6796047320988860$, $\mu_T = 1.415270827756886$ ($\varphi_T \simeq 54.8^\circ$), corresponding to $\alpha_T = 2.487161163767182 \simeq 142.5^\circ$), in which shoulder sliding and inner sliding activations may happen to occur together, thus also allowing for a direct shift between purely-rotational and purely-sliding modes.
- The upper part of the plot, say for arch states with thickness-to-radius ratio η around 1 and above, up to the physically maximum value of $\eta = 2$ ($t = 2r$), are marked by states with $\beta_r = 0$, in which the inner rotational joint pulls back to the crown, a characteristic feature that was first revealed, for a correct Heyman-like purely-rotational solution, in mentioned earlier work [10] (see here top plot in Fig. 3). Below, this is marked by an (almost horizontal) asymptotic line, rather near to asymptote $\eta = 1$. Further, just underneath of it, very closely, one other similar transition line (also almost horizontal and near to asymptote $\eta = 1$) sets in the positioning hierarchy of inner rotational vs. sliding states, separating, at $\beta_r = \beta_s$, mixed rotational-sliding states with $\beta_r > \beta_s$ (below) and with $\beta_r < \beta_s$ (above).
- The role of variable half-opening angle α , implicitly present within the two-dimensional projection plot, is highlighted by lines at constant α , which are apt to describe the variation of the arch characteristics at variable friction coefficient μ , at such given α (diverse peculiar and sample values of α are considered, and marked, within the plot). Specifically, coming from the right, at infinite μ , associated just to purely-rotational collapse modes and notwithstanding states with $\eta < 1$, a reducing, finite-value, friction coefficient, at constant η , may lead to encounter a first sliding activation, either at the shoulder (below the “Triple point”) or at an inner joint (above the “Triple point”).
- The transition lines, among the sliding activations, as ruled by a reducing μ , at resulting increasing η , are also marked, between the labelled separating dorsals. Then, at constant α , coming from the right, for $\eta < 1$, horizontal lines at constant η , hit either the shoulder

activation dorsal or the inner sliding activation dorsal, then get inclined, steeper below the “Triple point”, flatter above the “Triple point” (appearing as sorts of hyperbolas), and finally get vertical, at undefined supercritical η , once both sliding activations are met (purely-sliding modes).

- In the thick-arch $1 < \eta < 2$ range, hyperbola-like lines define the continuous transition from purely-overturning states at $\mu \rightarrow \infty$, and overturning-sliding states with inner sliding, as ruled by a finite, reducing μ , at slightly-increasing η (hyperbola-like curves get flatter and flatter at resulting increasing η and subjacent α).
- Notice that the right boundary of the plot, is truly represented only for $\mu \rightarrow \infty$ (namely $\varphi = 90^\circ$). Having chosen to represent friction states by friction coefficient μ , unbounded friction shall be seen just at very far right (East). Thereby, the Limit value of half-opening angle α that can be represented within the plot, thus within the overall analysis, results to be $\alpha_L = 2.786498150651177$ (about 160°), corresponding to $A(\alpha) = \alpha \cot(\alpha/2) = 1/2$, at reaching concomitant limits $\mu \rightarrow \infty$ and $\eta \rightarrow 2$.
- One subtle analytical point that was discovered, here worthwhile to be mentioned, as labelled in the analytical indications marked inside Fig. 6, is that, while for the classical purely-rotational Heyman-like (correct) solution, either non-dimensional horizontal thrust, “Lower” $h_1 = h_L$, or “Upper” h_U , may be adopted within the governing rotational equations [14] (thus either $h = h_1 = h_L$ or $h = h_U$, whereby equation $h = h_1 = h_L$ may be preferred for higher analytical simplicity), at infinite or super-critical (no sliding occurrence) friction, in the realm of mixed rotational-sliding is the role of h_U instead of $h_1 = h_L$ that shall be highlighted, to achieve correct results. This is because inner sliding activation occurs, and this “breaks” the upper portion of the half-arch, in representing the inner rotational equilibrium from above (with respect to the inner hinge at the haunch); thus, the inner rotational equilibrium shall correctly be represented from below, through h_U .
- Conversely, on the left of the “Triple point”, while up above the lower interface marking shoulder sliding activation at $\mu = \mu_{ss}$ (and down below the upper interface marking additional inner sliding activation at $\mu = \mu_{is}$), thrust h_U , in the meaning of inner rotational equilibrium of the below part of the half-arch, cannot be used, while $h_1 = h_L$ must be adopted, given the sliding activation at the shoulder in arising mixed sliding-rotational modes (with sliding at the shoulder, of the bottom part of the half-arch, and rotation at the inner joint, of the upper part of the half-arch).

Out of the above analytical treatment, and representation, the family of contemplated failure mechanisms of the symmetric circular masonry arch at variable inherent friction comprises the following seven collapse modes [with indication of joints’ type, among rotational (r) or sliding (s), raising from shoulder]:

- purely-rotational (classical, correct, Heyman-like one) [r,r,r];
- purely-sliding [s,s];
- mixed sliding-rotational (with shoulder sliding) [s,r,r];
- mixed rotational-sliding (with inner sliding), with $\beta_r \geq \beta_s$ [r,r,s];

- mixed rotational-sliding (with inner sliding), with $\beta_r \leq \beta_s$ [r,s,r];
- overturning-sliding ($\beta_r = 0$, with inner sliding and no block separation at the crown), for finite μ , at non-zero horizontal thrust h ruled by μ [r,s];
- purely-overturning ($\beta_r = 0$, with two-block separation at the crown), for infinite μ and $1 \leq \eta \leq 2$, at zero horizontal thrust h [r].

Figs. 9-11 further depict the analytical domains of the arch states in main $\eta\text{-}\mu$ filled plots, again at implicitly variable half-opening angle α , with analytical indications (Fig. 9), or not (Fig. 10), and appropriate zoom (Fig. 11), to appreciate characteristic shifts in the central part, where six main regions are accordingly shaded, with collapse ruled by the following modes:

- purely-rotational (South-East);
- purely-sliding (North-West);
- mixed sliding-rotational, with shoulder sliding (inner “pond” among the above, up to a characteristic “Triple point”);
- mixed rotational-sliding, with inner sliding (lower North-East “basin”, still among the above, after such a “Triple point”, upper bounded by condition $\beta_r = 0$, with manifested asymptotic trend for $\eta \rightarrow 1$ as $\mu \rightarrow \infty$);
- latter domain formally subdivided into two shaded regions, with $\beta_r \geq \beta_s$, below, and, very thin slice, with $\beta_r \leq \beta_s$, above;
- overturning-sliding (upper North-East “basin”, lower bounded by condition $\beta_r = 0$ and upper bounded through limit $\eta \leq 2$);
- additionally, not directly visible in the filled plot, for $\mu \rightarrow \infty$, far-East boundary segment of purely-overturning modes at unbounded friction, for $1 \leq \eta \leq 2$.

The characteristics of the landmark points coming to appear along the main “continental divide” in the $\eta\text{-}\mu$ plots, going from South-West to North-East, from $\eta = 0$ to $\eta = 2$, separating the arch states with collapse modes that do not (left) or do (right) display rotation (Fig. 9) are reported in Table 1, for the ease of reference.

	(T) Triple point	(S) Shift point	(J) Junction point	(B) Border point
η	0.6796047320988860	0.9533663968209255	0.9652414772084208	2
μ	1.415270827756886	1.765868462744654	1.777213608388237	2.690297881776622
α	2.487161163767182	2.600211150484514	2.603266515104794	2.774176793356034
h	0.09780581933963814	0.06791978142522512	0.06718190191428895	0.03200476409857036
β_r	1.037485213550072	0.2516081968386061	0	0
β_s	0.2970519164101457	0.2516081968386061	0.2503367611228279	0.1760126676508405

Table 1: Characteristic data of peculiar landmark points along the divide in the $\eta\text{-}\mu$ plane.

The $\eta\text{-}\mu$ filled plot in Fig. 9 contains the pertinent analytical information, consistently with what earlier done in Fig. 6. The two analytical plots in Figs. 6 and 9, with therein reported analytical indications, shall constitute the main analytical outcome of the present contribution, in the attempt of describing the role of finite friction and relevant arising finite-friction effects.

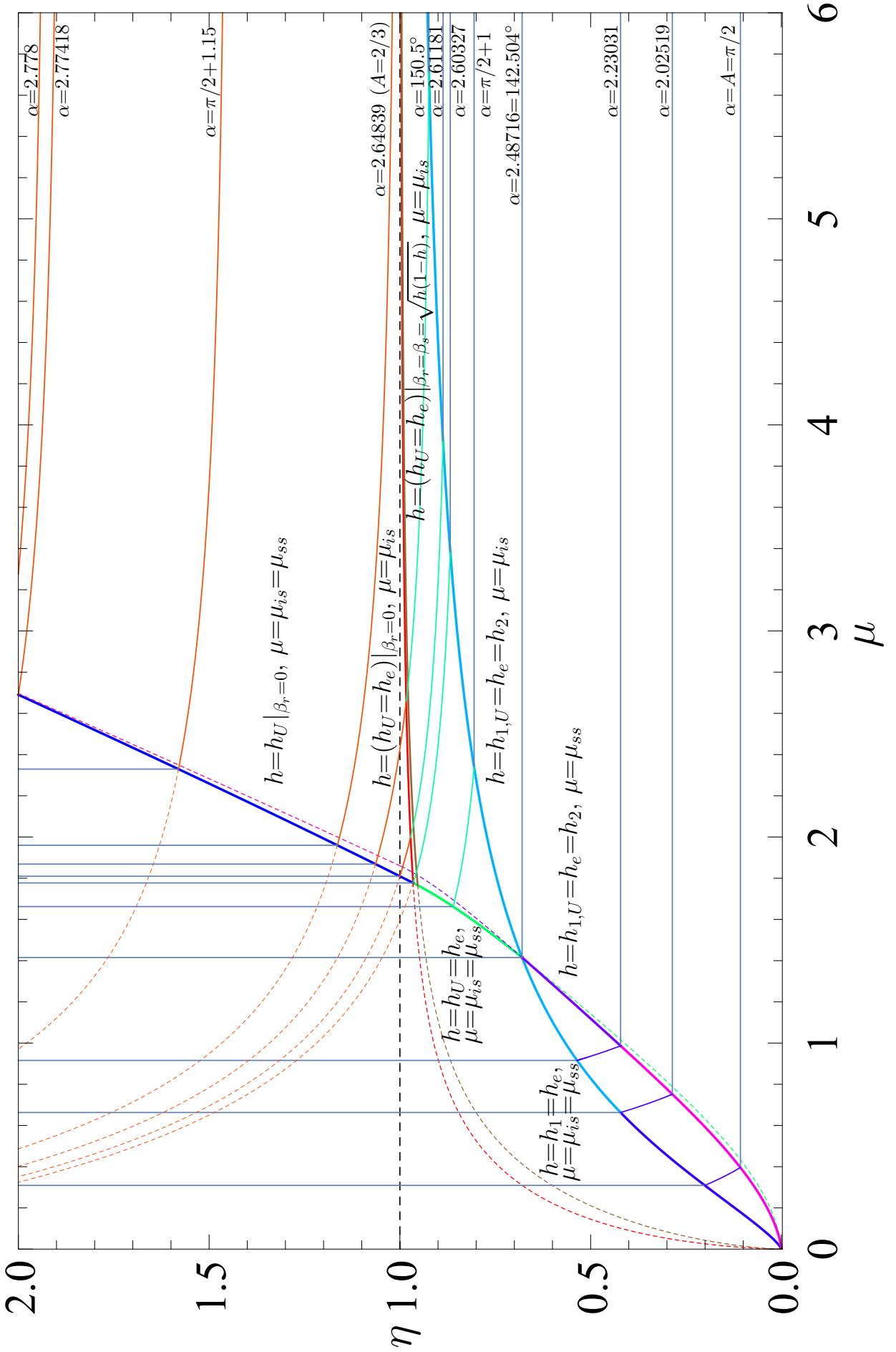


Figure 6: Analytical η - μ map of self-standing and collapse states, for all admissible $0 \leq \eta \leq 2$.

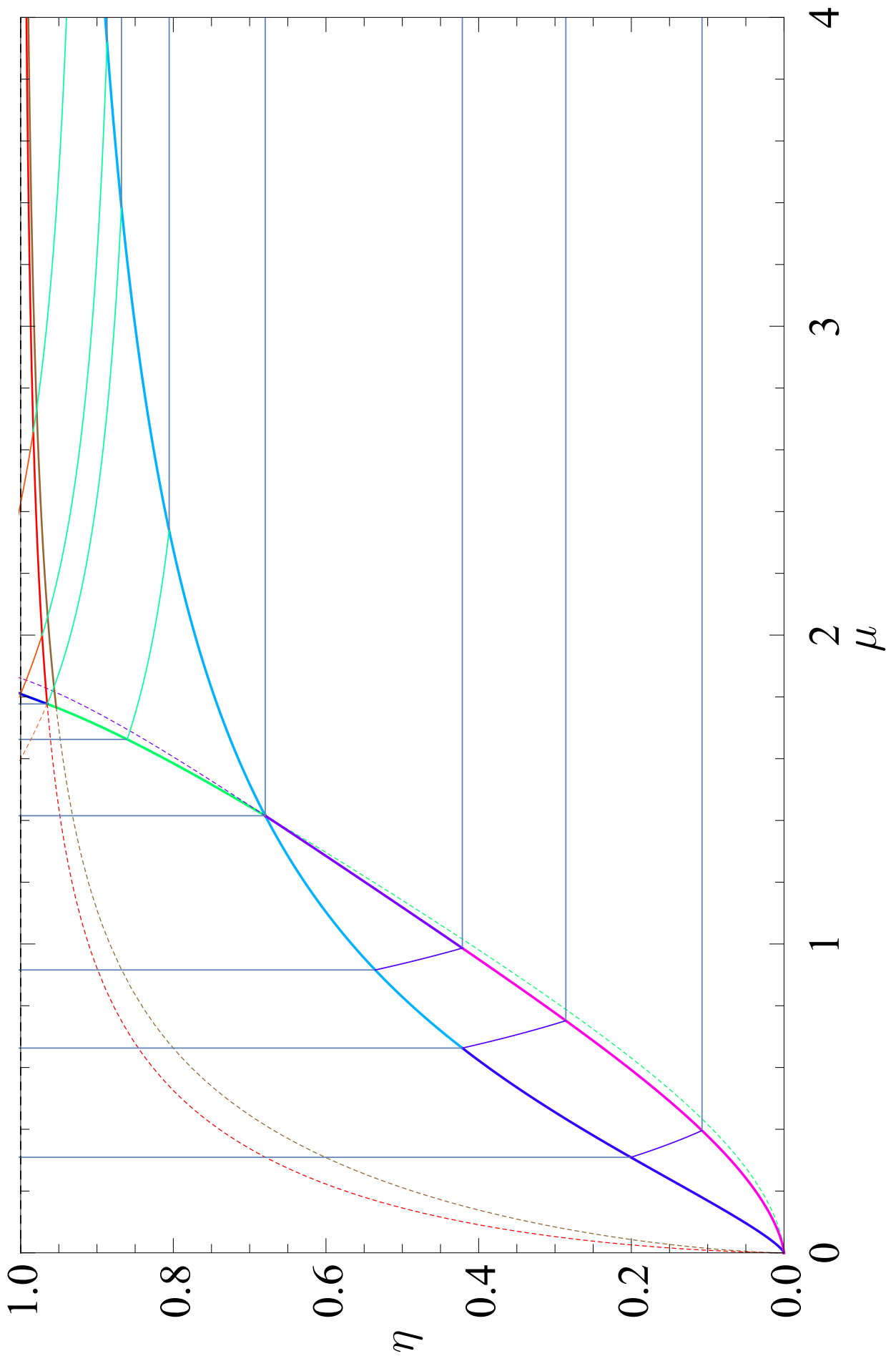


Figure 7: Analytical η - μ map of self-standing and collapse states: $0 \leq \eta \leq 1$ zoom.

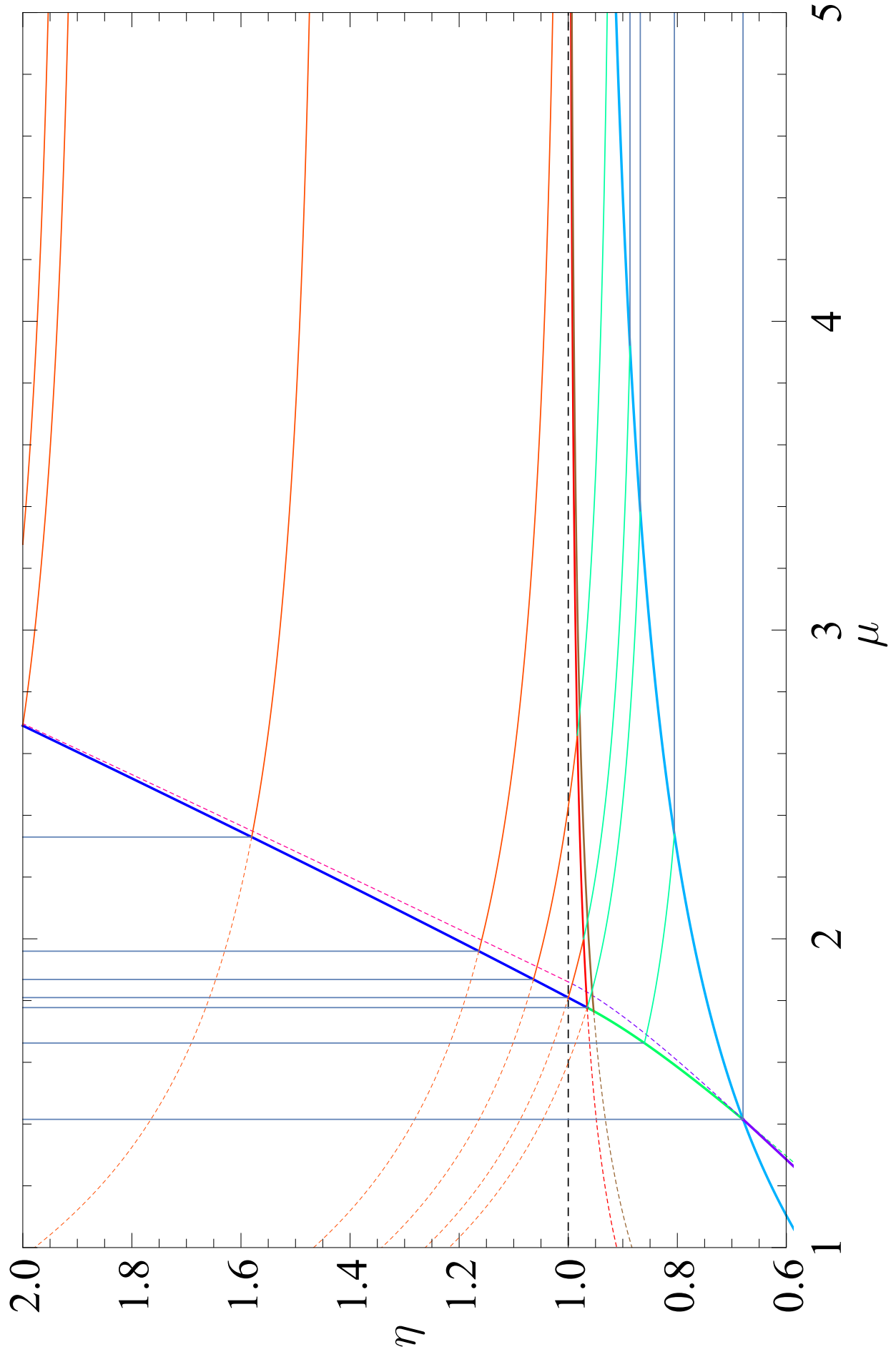
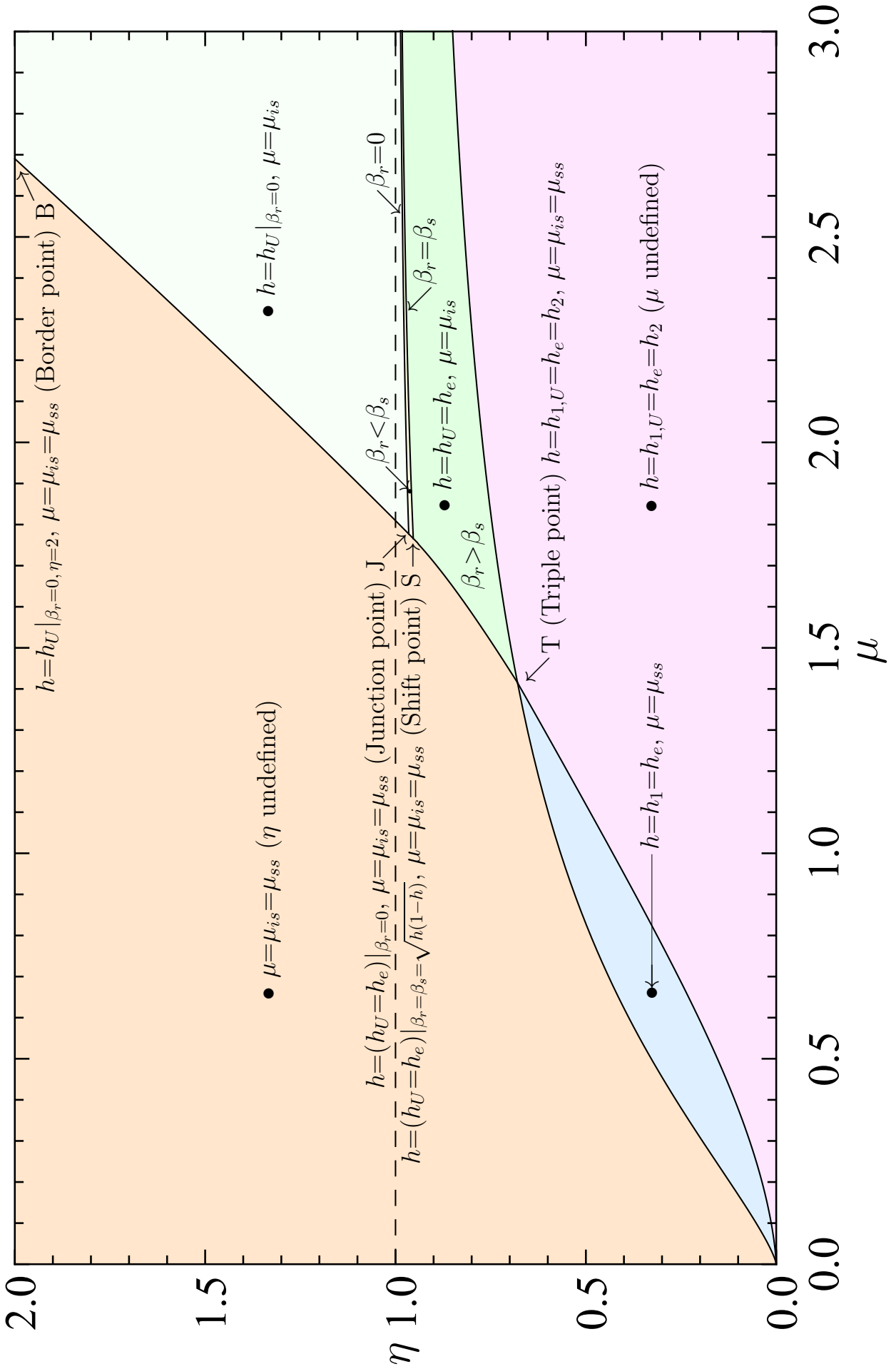


Figure 8: Analytical η - μ map of self-standing and collapse states: $0.6 \leq \eta \leq 2$ zoom.



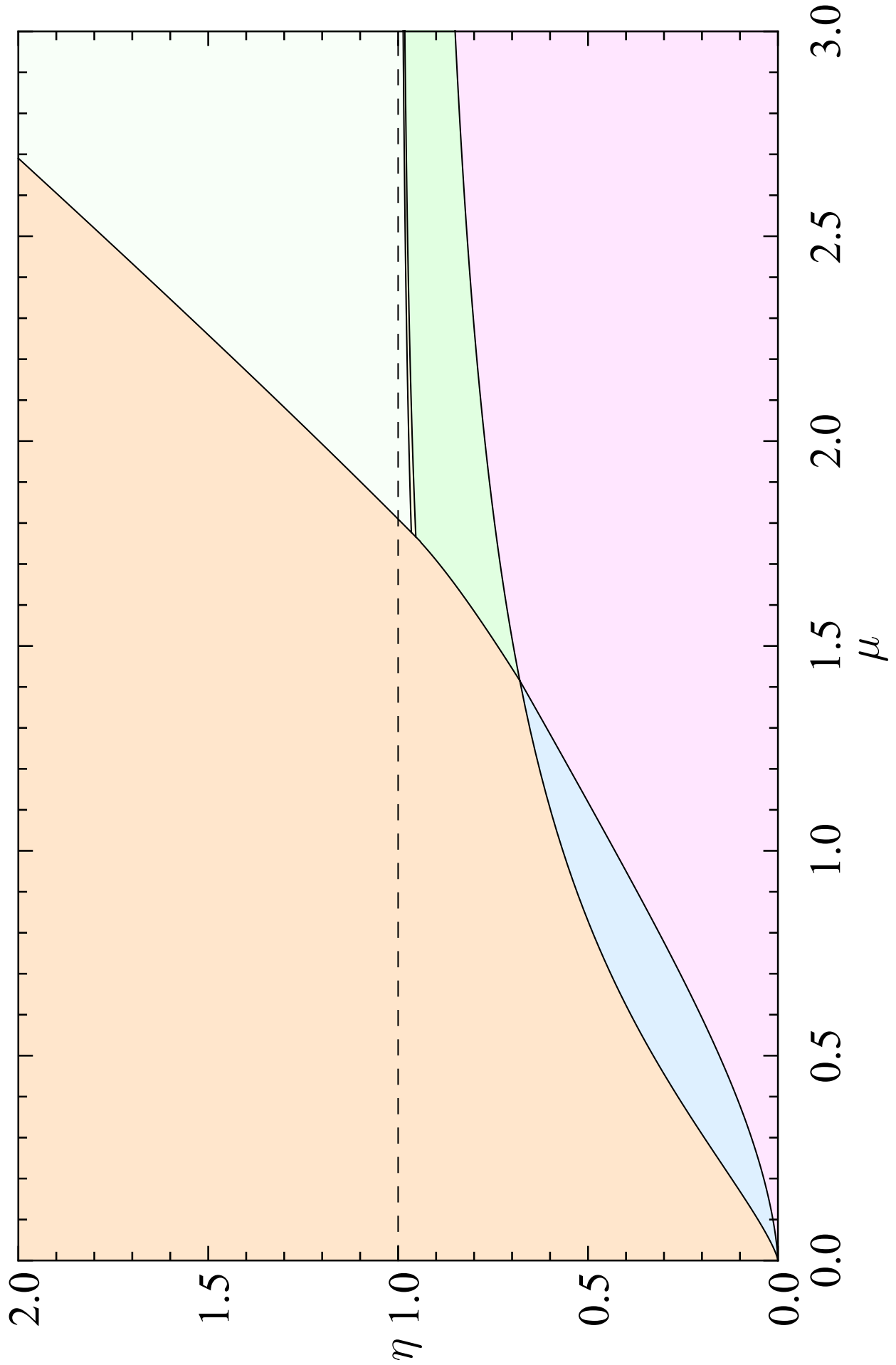


Figure 10: Filled η - μ domains of self-standing and collapse states.

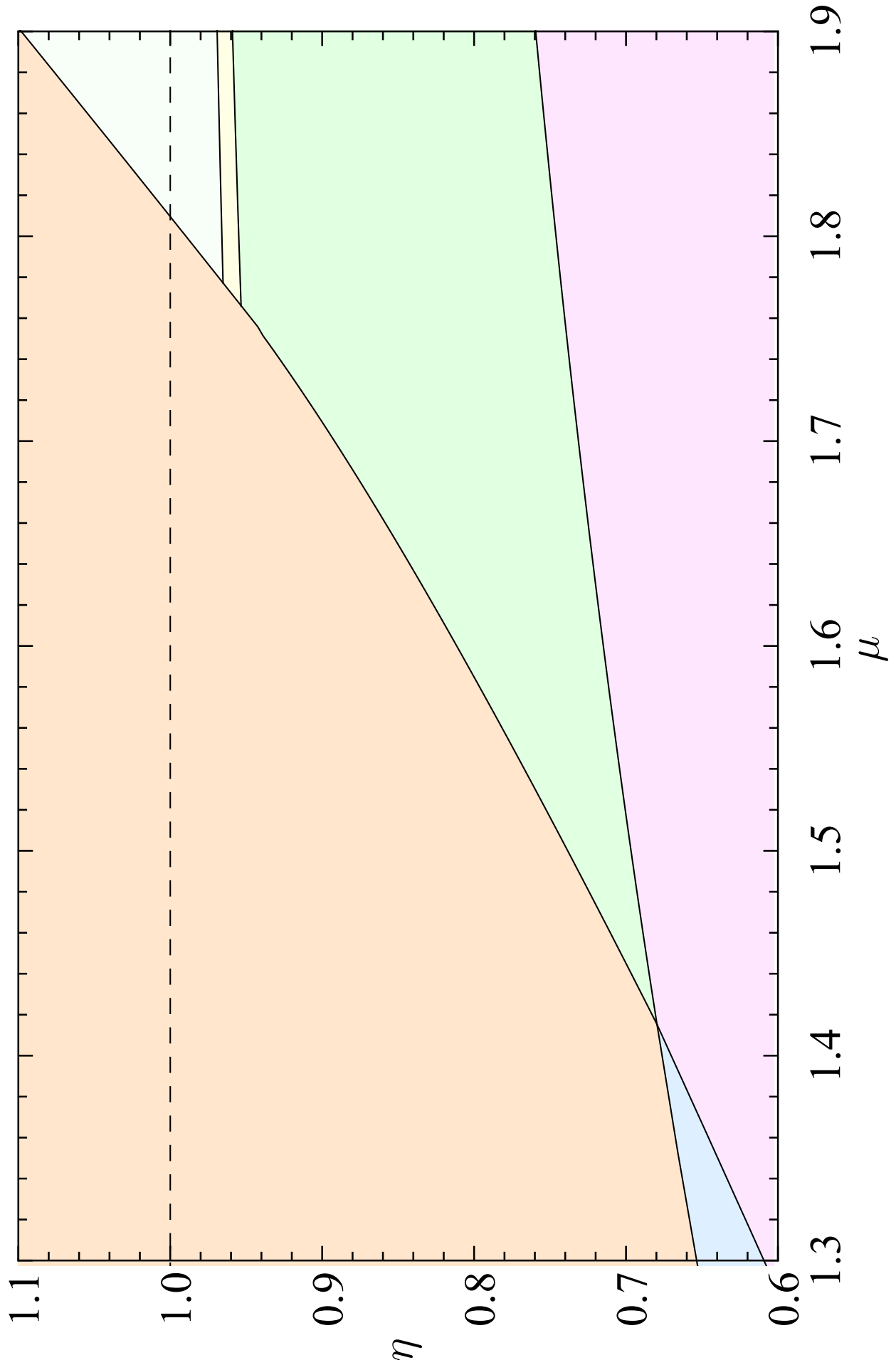


Figure 11: Filled η - μ domains of self-standing and collapse states: central zoom.

3.1 Resuming remarks and physical implications

From the achieved main analytical η - μ representations, the following salient interpretation remarks and physical implications may be in order (resulting wholly consistent with earlier preliminary finite friction results [20, 56, 64], and going much beyond):

- Coming from the right, at a reducing friction coefficient $\mu = \tan \varphi$, in the $0 \leq \eta \leq 1$ range, the encounter with the East boundary separating purely-rotational collapse modes and mixed (sliding-rotational or rotational-sliding) mechanisms marks, at increasing half-opening angle of the arch α , an increasing friction coefficient μ and an increasing thickness-to-radius ratio η necessary to prevent sliding within the masonry arch.
- The characteristic “Triple point” at $\alpha_T = 2.487161163767182 \simeq 142.5^\circ$ (point T in Fig. 9), marking a direct switch from purely-rotational to purely-sliding modes, as well as a direct shift from sliding-rotational to rotational-sliding mechanisms, sets a sort of regional landmark, in the maps of the collapse states. In practice, arches with $\alpha \leq \alpha_T$ (most common cases) and $\mu \geq \mu_T = 1.415270827756886$ ($\varphi_T \simeq 54.8^\circ$, say about 55°) are prevented to show any sliding mode (think to reasonable third Heyman hypothesis of no sliding failure in practical cases). This may provide a sort of analytical quantification, on a conservative amount of required finite friction, in the classical Heyman sense of the third hypothesis of no sliding failure.
- All separating boundaries, of the collapse domains, require a decreasing trend of thickness-to-radius-ratio η at decreasing friction coefficient μ (and concomitant decreasing half-opening angle α), meaning that, at these transitions, a reducing friction coefficient requires a diminution of least thickness.
- Overturning-sliding modes, with sliding around the crown, at finite friction appear in the region around $\eta = 1$ and beyond, up to $\eta = 2$, for rather opened arches. These overturning modes with additional sliding anyhow appear for a friction coefficient that shall be larger than value $\mu_J = 1.777213608388237$ ($\varphi_J \simeq 60.6^\circ$), recorded at a “Junction point” (point J in Fig. 9).
- Purely-overturning modes, at zero non-dimensional horizontal thrust, $h = 0$, arise just at infinite friction coefficient, $\mu \rightarrow \infty$, for $2.648388899151007 \leq \alpha \leq 2.786498150651177$ (say $152^\circ \leq \alpha \leq 160^\circ$), namely for $2/3 \geq A(\alpha) = \alpha \cot(\alpha/2) \geq 1/2$, and with $1 \leq \eta \leq 2$, representing a rather precarious equilibrium state at incipient collapse whereby the line of application of the resultant self-weight of the half-arch is exactly aligned with the underneath extrados hinge at the shoulder. Infinite friction is necessary, thereby, to avoid additional half-arch breaking, by sliding, around the crown.
- Given the far-East “Border point” extremity of the purely-sliding domain at the intersection of its East boundary with upper border $\eta = 2$ (point B in Fig. 9), occurring for $\alpha_B = 2.774176793356034 \simeq 159^\circ$ and $\mu_B = 2.690297881776622$ ($\varphi_B \simeq 69.6^\circ$), a value of friction coefficient that shall be larger than that (say friction angle larger than about 70°) shall prevent any purely-sliding mode to appear within the masonry arch.

4 Illustration/validation by a numerical CP/MP formulation

A final separate illustration by a Complementarity Problem/Mathematical Programming formulation, as a numerical validation and cross-corroboration of the achieved analytical results is then pursued. For the visual illustration of the characteristic features of the previous rigorous analytical analysis, and also toward independent numerical validation of the achieved analytical predictions, an original CP/MP computational approach can be adopted, as formulated in [13, 14], to deliver and depict all final results corresponding to the self-standing domains and collapse conditions that have earlier been derived on an analytical basis.

As a main general concept, as classically outlined in the Theory of Plasticity, of both Solids and Structures, the masonry arch states can be ruled by a Complementarity Problem formulation, among strength conditions within static internal variables φ and collapse kinematic variables at rotating/sliding joints $\dot{\lambda}$ (Fig. 12), which can be brought down to a Mathematical Programming problem under linear constraints, where the quest of a numerical zero in the solution may even come out in the order of 10^{-16} , to clearly outline the onset of collapse:

$$\text{CP: } \varphi \leq \mathbf{0}, \quad \dot{\lambda} \geq \mathbf{0}, \quad \varphi^T \dot{\lambda} = 0 \quad (15)$$

\Downarrow

$$\text{MP: } \min \left\{ -\varphi^T \dot{\lambda} \mid \text{lin. constr.} \right\} = 0 \quad (16)$$

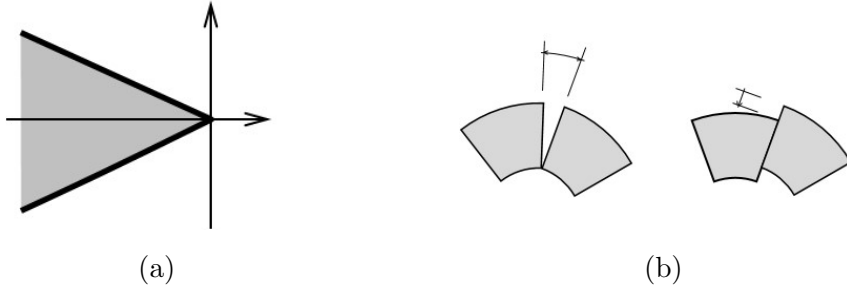


Figure 12: (a) Strength conditions within static internal variables $\varphi \leq \mathbf{0}$; (b) Collapse kinematic variables at rotating/sliding joints $\dot{\lambda} \geq \mathbf{0}$.

Such a “ φ - λ formulation”, self-implemented within MatLab (see computational details in [13, 14]), turns out particularly feasible, in the present setting of tracing masonry arch mechanisms, to locate and depict the collapse modes that are reached in the least-thickness (or sub-critical thickness) condition, at given geometrical morphology and variable inherent friction among the theoretical blocks of the arch. Basically, geometrical and characteristic features are exactly revealed by the earlier analytical analysis, then implemented within the numerical code, to achieve additional confirmation and, most of all, pertinent physical illustration of the resulting solution. In the present case, of symmetric circular masonry arches, the collapse mechanisms coming from the solution of Eq. (16) in terms of $\dot{\lambda}$ is set from scratch to turn out symmetric.

As a main resuming outcome, Figs. 13-25 report typical masonry arches and collapse modes that may be obtained for characteristic half-opening angles and friction coefficients, as associated to the previous η - μ representations in Figs. 6-8 (see analytical lines and displayed “iso- α ” curves) and Figs. 9-11 (see filled regions and characteristic points), and attached mathematical and physical description in the previous sections, all together showing: geometrical features of the arch in the least-thickness condition (black); strictly all-internal line of thrust (red) and line of friction (blue); symmetric associated collapse mode, possibly including sliding (green).

Specifically:

- Figs. 13-17 report two different arch instances with possibly arising mixed modes, for given values of half-opening angle α , and variable characteristic friction coefficient μ , respectively leading into the “pond” of mixed sliding-rotational modes ($\alpha = 125^\circ \simeq 2.181661564992912$) and in the “basin” of mixed rotational-sliding modes ($\alpha = 145^\circ \simeq 2.530727415391778$). Thereby, Figs. 13-14 and 15-16 show the four configurations arising at the sliding interfaces in the η - μ plots, at those two “iso- α ” values, and Fig. 17 displays a direct comparison between a mixed sliding-rotational mode for $\alpha = 125^\circ$ and a mixed rotational-sliding mode for $\alpha = 145^\circ$, at given “rounded” values of μ , respectively $\mu = 0.9$ ($\varphi \simeq 42^\circ$) and $\mu = 1.6$ ($\varphi \simeq 58^\circ$), within “pond” and “basin” of the η - μ filled plots.
- Figs. 18-19 show the characteristics associated to the landmark, “Triple point”, in the η - μ plot, separating mixed sliding-rotational and mixed rotational-sliding modes, where also a direct shift from purely-rotational to purely-sliding modes is rejoined. Thereby, Fig. 18 depicts the shift from purely-rotational to purely-sliding mode, while Fig. 19 illustrates the shift from mixed sliding-rotational to mixed rotational-sliding mode. In practice, four physical modes are concomitantly represented at point T of the η - μ plane (Fig. 9), while the relevant mechanisms shall mathematically be obtained by any linear triple combination of three of them.
- Figs. 20-22 display the arch features for $\alpha_J = 2.603266515104794 \simeq 149.2^\circ$, along the “hyperbola-like” line at constant $\alpha = \alpha_J$ reaching the “Junction point” where condition $\beta_r = 0$ is first met raising along the South-West/North-East “continental divide” in the η - μ plots. Thereby, Fig. 20 reports concomitant mixed rotational(overturning)-sliding (with $\beta_r = 0$) and purely-sliding mode at the “Junction point”. Fig. 21 depicts an instance with $\beta_r < \beta_s$ (where β_r is about 1/2 of β_s), within the thin slice of the shaded region better seen in Fig. 11, and peculiar case $\beta_r = \beta_s$, corresponding to the intercept with line $\beta_r = \beta_s$ at that $\alpha = \alpha_J$ (thereby, the inner joint displays sliding plus rotation). Fig. 22 shows the arch representation for the lower intercept with the line of inner sliding activation, with resulting rotational-sliding (with $\beta_r > \beta_s$) and purely-rotational modes at that interface (around $\mu \simeq 3.4$ and $\eta \simeq 0.87$).
- Fig. 23 illustrates the arch corresponding to $\eta = 1$ and $\alpha = 2.611810358168302 \simeq 149.6^\circ$ at $\mu \simeq 1.8$, where the above “continental divide” meets condition $\eta = 1$ (dashed horizontal line and asymptote in the η - μ plots), with shift from overturning-sliding to purely-sliding mode.
- Fig. 24 corresponds to the “Border point” with $\alpha_B = 2.774176793356033 \simeq 158.9^\circ$ and $\mu \simeq 2.7$, where the dorsal reaches upper feasible limit $\eta = 2$ ($t = 2r$), with shift from overturning-sliding to purely-sliding mode.
- Fig. 25 depicts two sample, characteristic instances of purely-overturning mode, for $\eta = 1$ ($\alpha = 2.648388899151005 \simeq 151.7^\circ$, at $A = 2/3$), and $\eta = 2$ ($\alpha = 2.786498150651177 \simeq 159.7^\circ$, at $A = 1/2$), on the extremities of the right boundary segment at $\mu \rightarrow \infty$ ($\varphi = 90^\circ$) for $1 \leq \eta \leq 2$.

In practice, the collapse modes depicted in Figs. 13-25, highlight characteristic samples offering a comprehensive panorama of all the failure mechanisms that can be experienced in the six shaded regions in the η - μ filled plots, plus the seventh region constituted by the segment on the right limit boundary at $\mu \rightarrow \infty$ ($\varphi = 90^\circ$), for $1 \leq \eta \leq 2$.

This shall provide a comprehensive mechanical view of the main characteristic features, for the considered least-thickness form-optimization problem of (symmetric circular) masonry arches (with radial joints), at reducing friction.

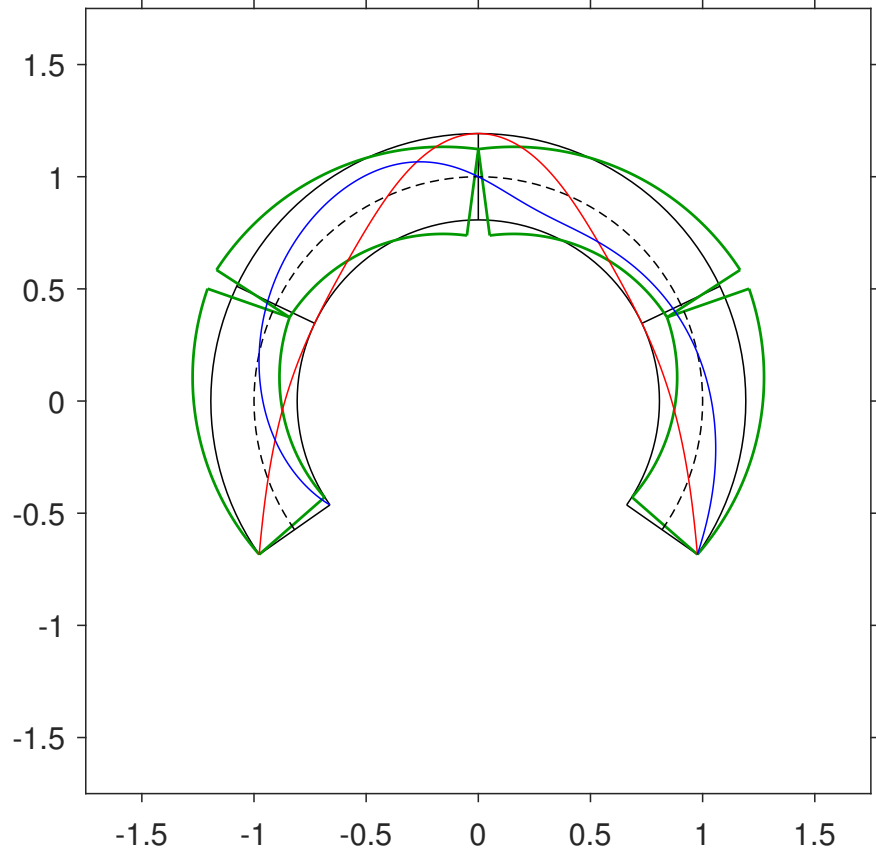
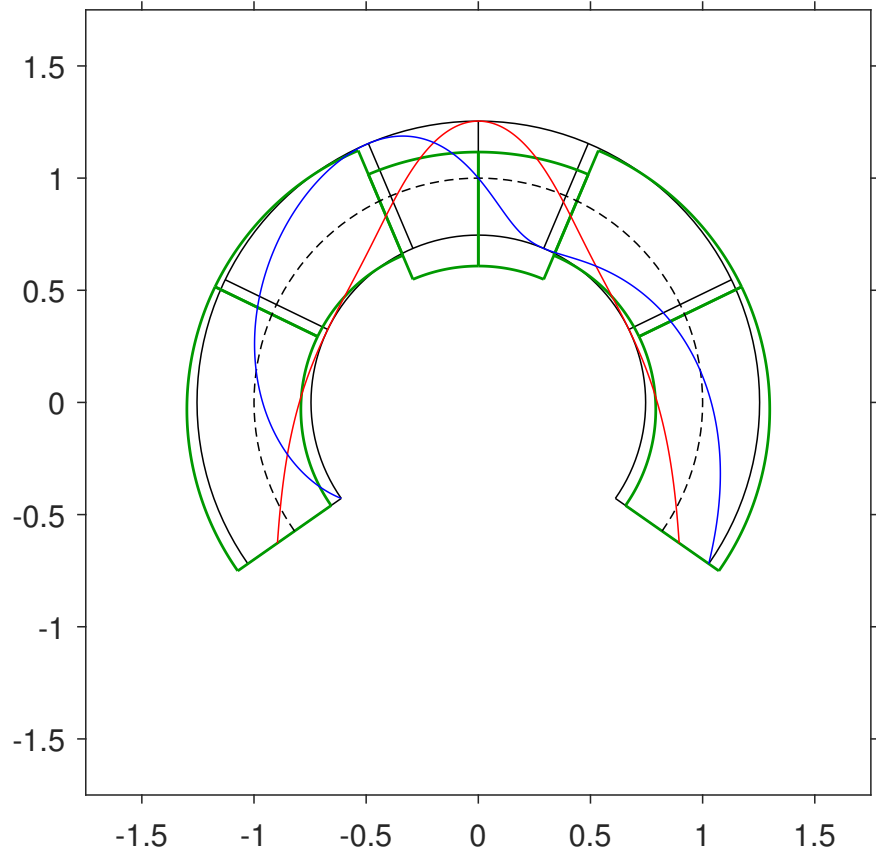


Figure 13: Least-thickness collapse mechanism, with line of thrust and line of friction:
 (top) purely-sliding, for $\alpha=125^\circ$, $\mu=0.8477497839674316$ ($\varphi \approx 40.3^\circ$), $\eta=0.5081418006878796$;
 (low) purely-rotational, for $\alpha=125^\circ$, $\mu=0.9245590639478306$ ($\varphi \approx 42.8^\circ$), $\eta=0.3849612500740051$.

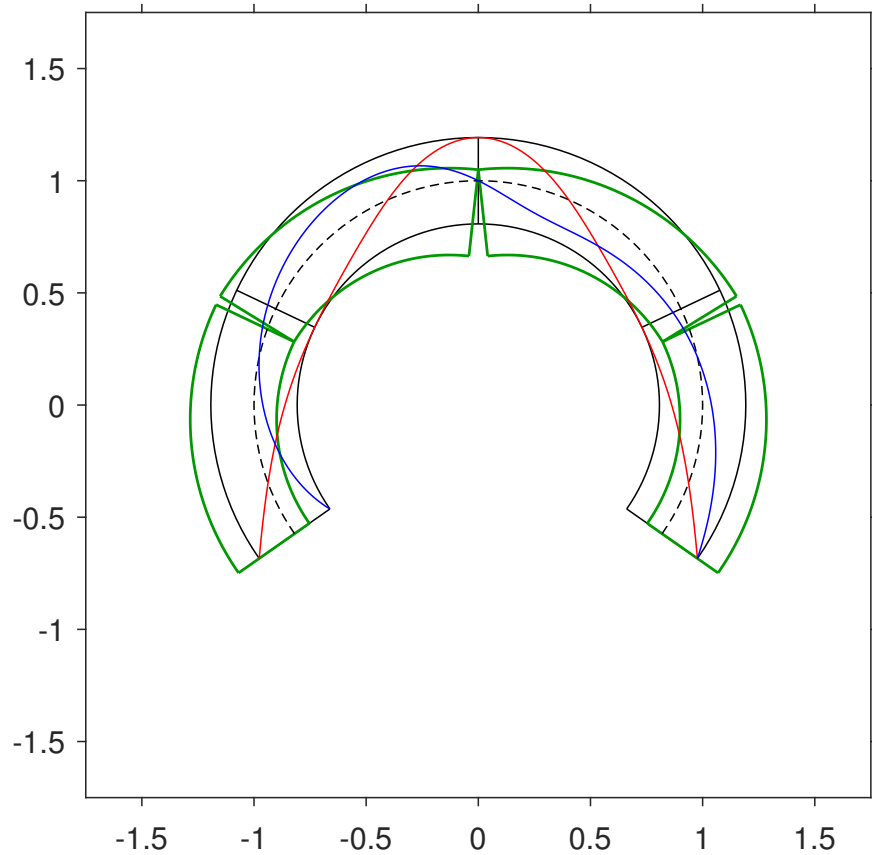
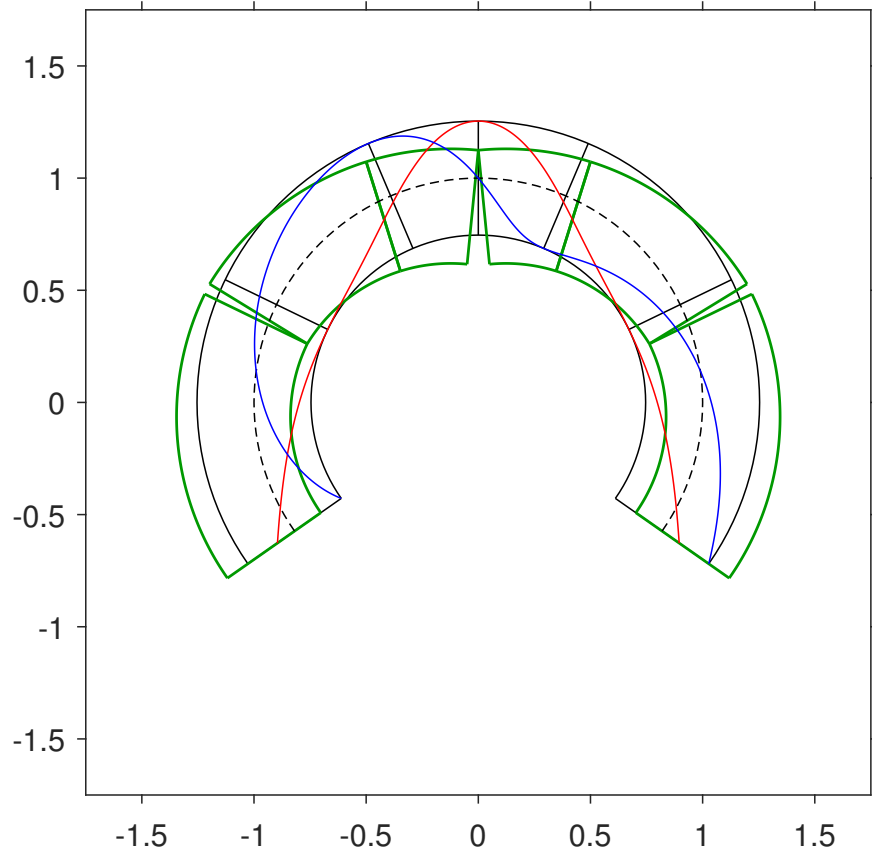


Figure 14: Least-thickness collapse mechanism, with line of thrust and line of friction:
 (top) sliding-rotational, for $\alpha=125^\circ$, $\mu=0.8477497839674316$ ($\varphi \approx 40.3^\circ$), $\eta=0.5081418006878796$;
 (low) sliding-rotational, for $\alpha=125^\circ$, $\mu=0.9245590639478306$ ($\varphi \approx 42.8^\circ$), $\eta=0.3849612500740051$.

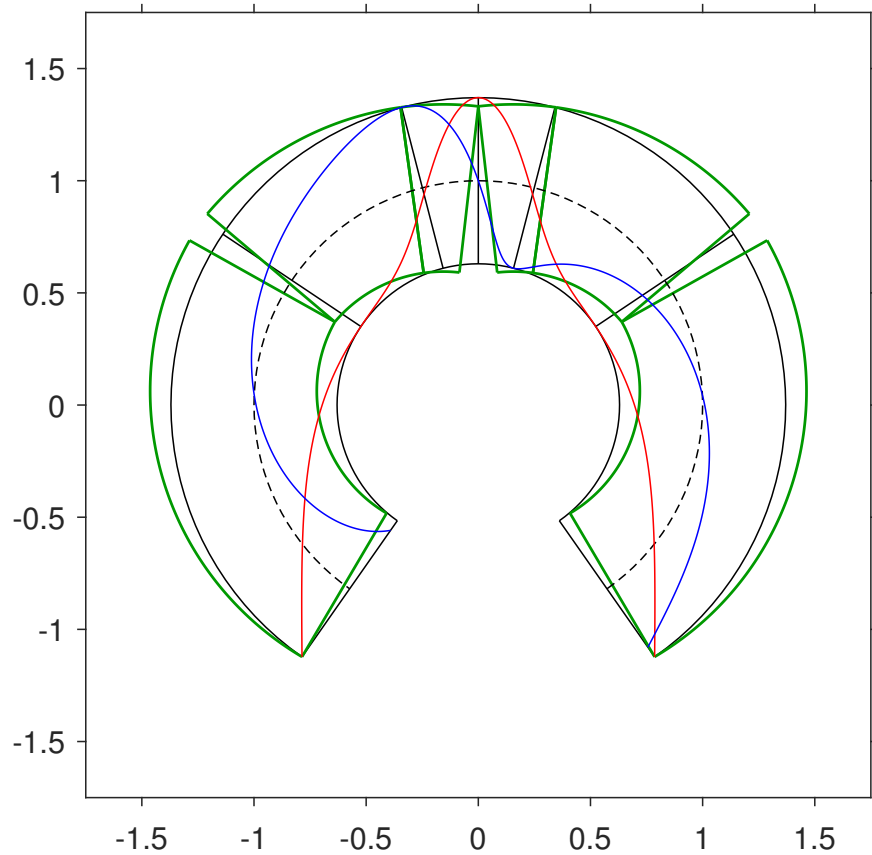
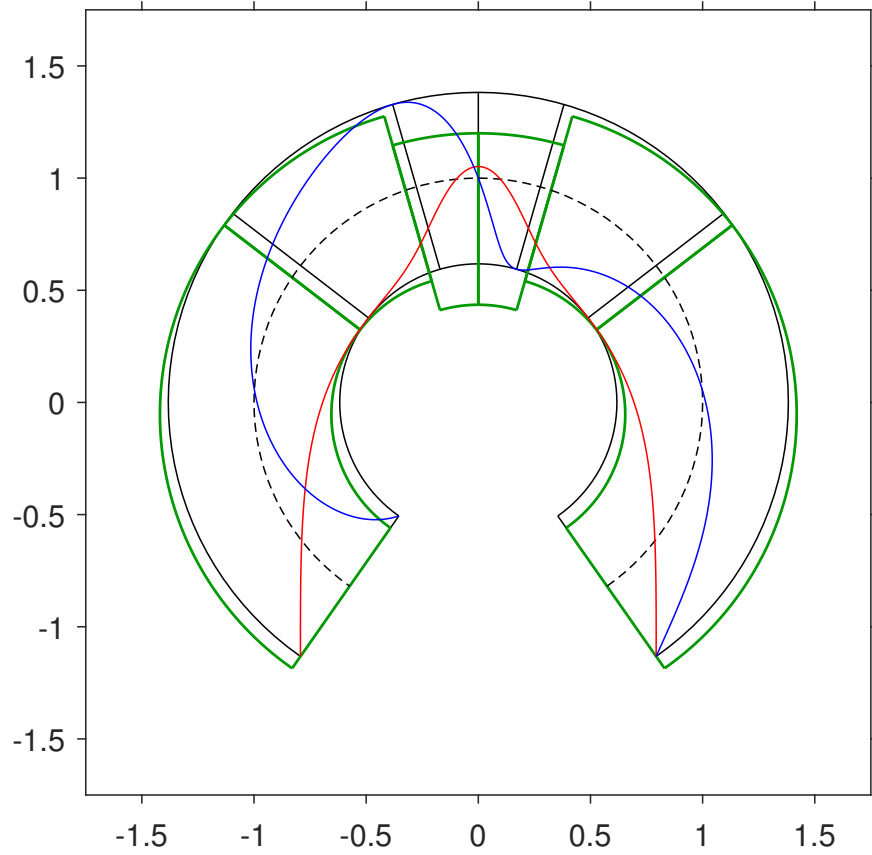


Figure 15: Least-thickness collapse mechanism, with line of thrust and line of friction:
 (top) purely-sliding, for $\alpha=145^\circ$, $\mu=1.536310506737699$ ($\varphi \approx 56.9^\circ$), $\eta=0.764335711953571$;
 (low) purely-rotational, for $\alpha=145^\circ$, $\mu=1.761938080825641$ ($\varphi \approx 60.4^\circ$), $\eta=0.7406376307743147$.

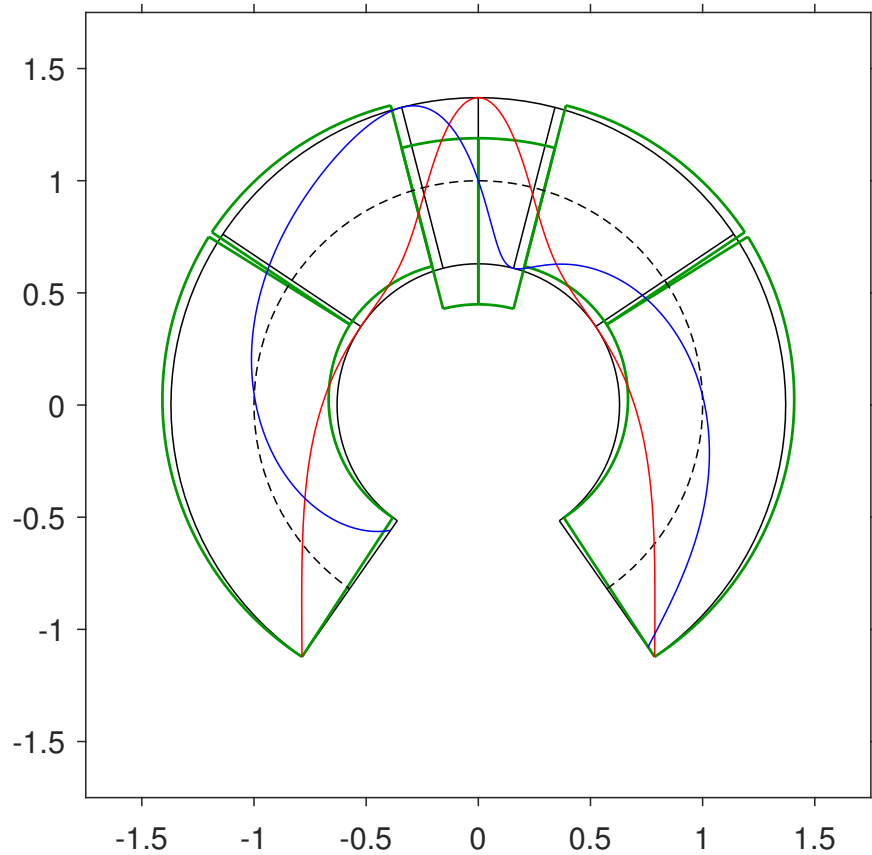
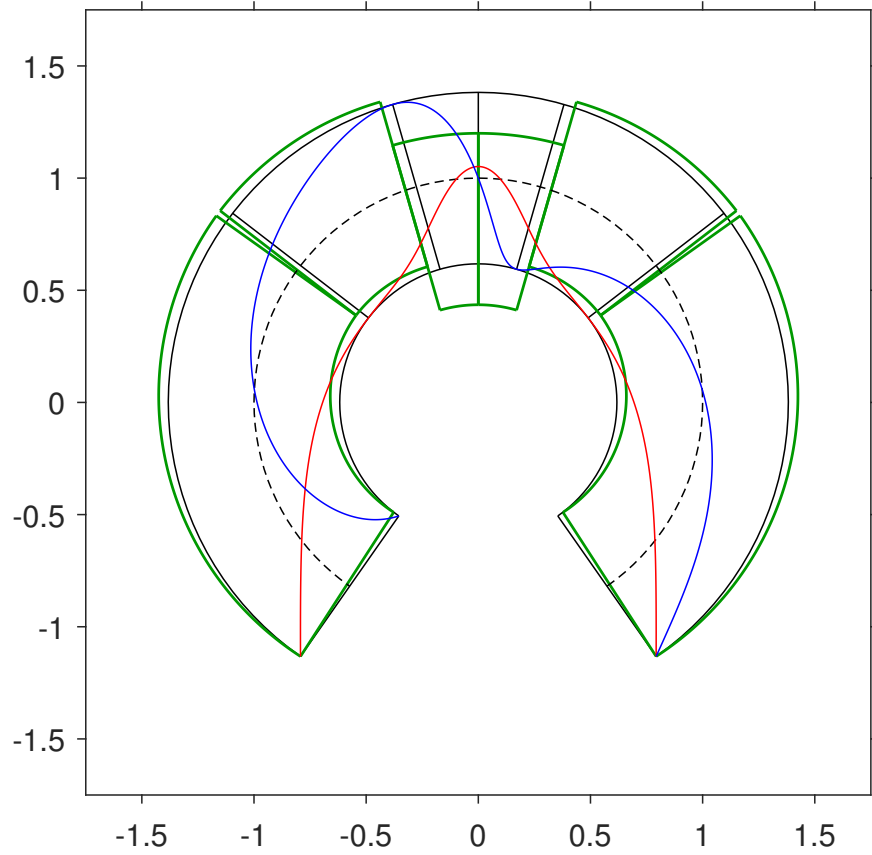


Figure 16: Least-thickness collapse mechanism, with line of thrust and line of friction:
 (top) rotational-sliding, for $\alpha=145^\circ$, $\mu=1.536310506737699$ ($\varphi \simeq 56.9^\circ$), $\eta=0.7643357111953571$;
 (low) rotational-sliding, for $\alpha=145^\circ$, $\mu=1.761938080825641$ ($\varphi \simeq 60.4^\circ$), $\eta=0.7406376307743147$.

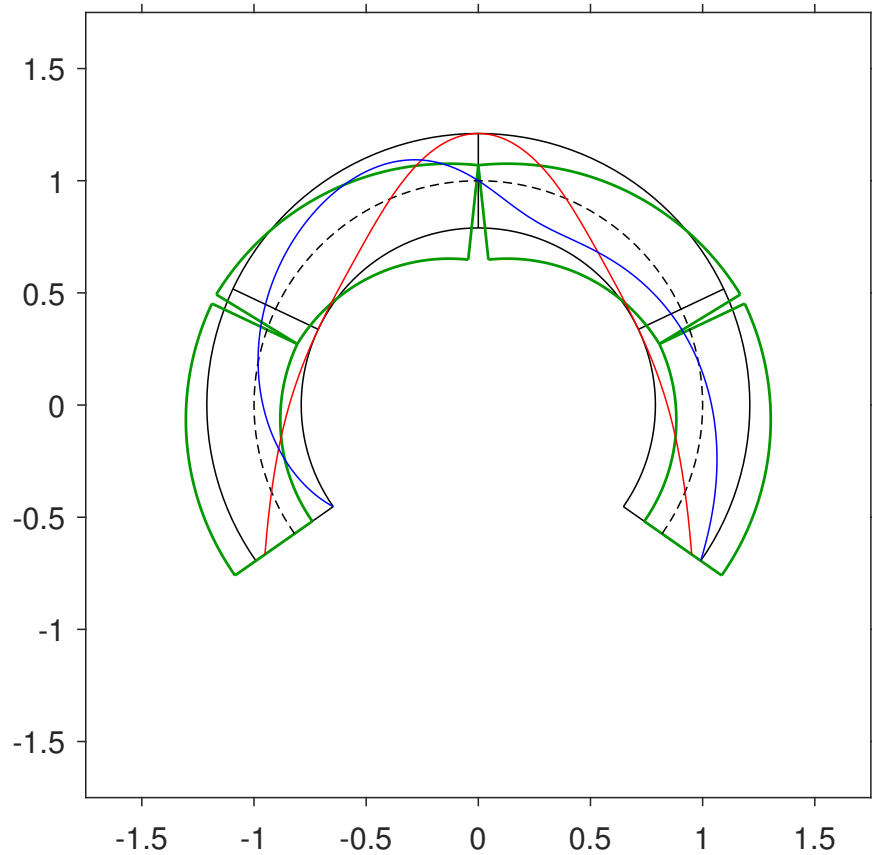
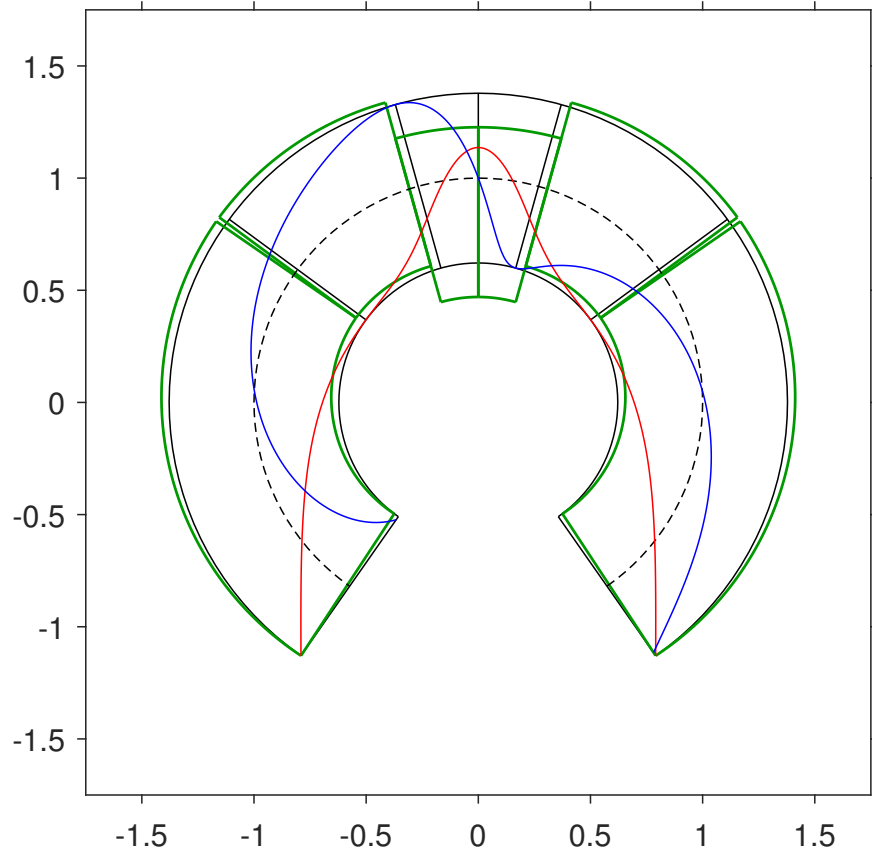


Figure 17: Least-thickness collapse mechanism, with line of thrust and line of friction:
 (top) rotational-sliding, for $\alpha=145^\circ$, $\mu=1.6$ ($\varphi \approx 58.0^\circ$), $\eta=0.7566761737936022$;
 (low) sliding-rotational, for $\alpha=125^\circ$, $\mu=0.9$ ($\varphi \approx 42.0^\circ$), $\eta=0.4208869235292454$.

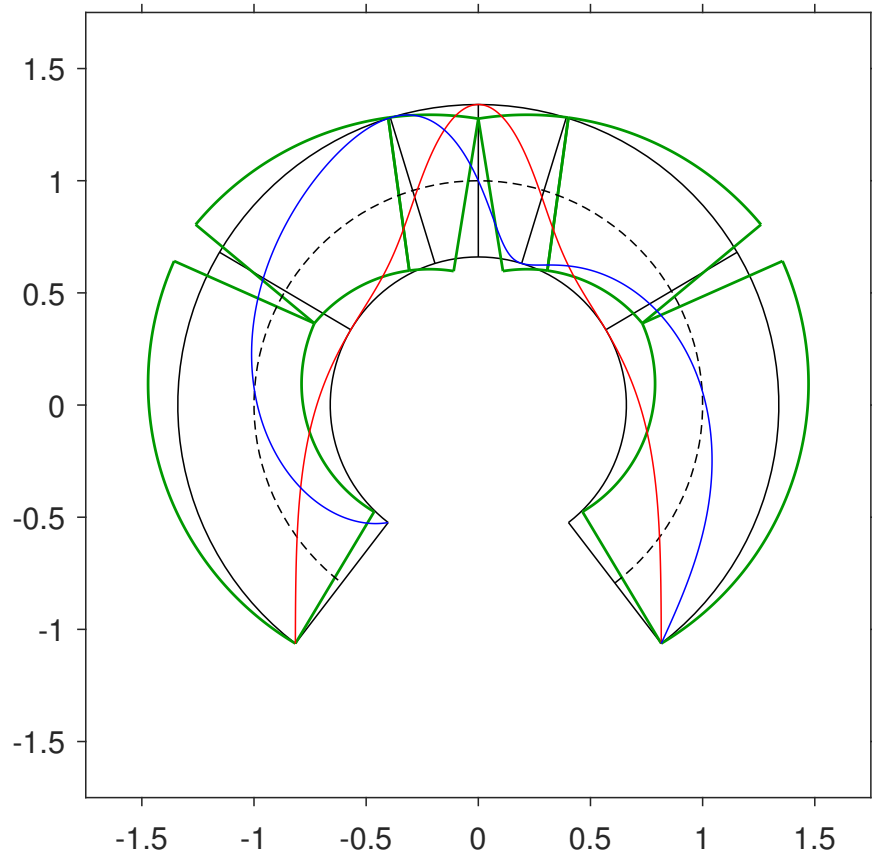
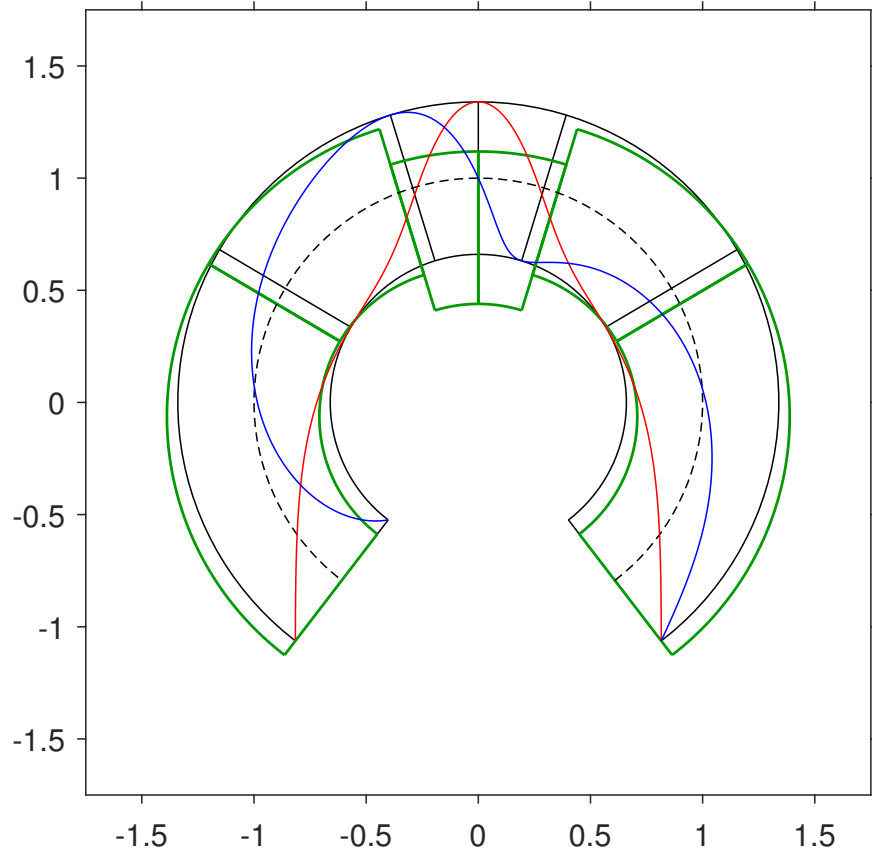


Figure 18: Least-thickness collapse mechanism, with line of thrust and line of friction: at “Triple point” with $\alpha_T = 2.487161163767182 \approx 142.5^\circ$, $\mu_T = 1.415270827756885$ ($\varphi_T \approx 54.8^\circ$), $\eta_T = 0.6796047320988855$: purely-sliding (top); purely-rotational (low).

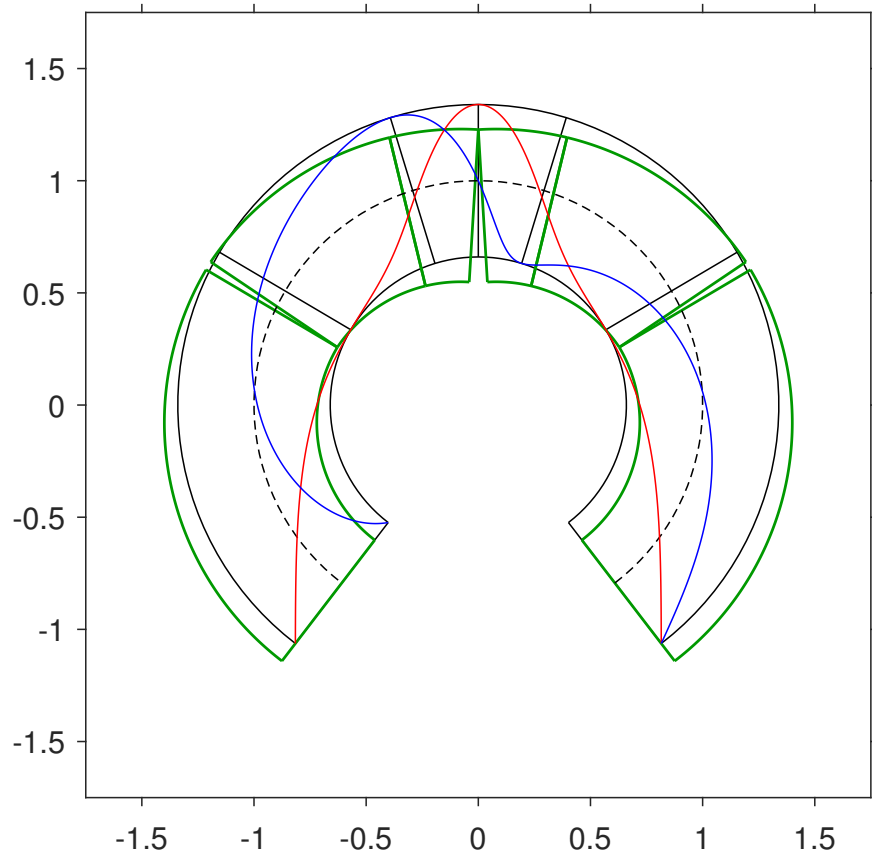
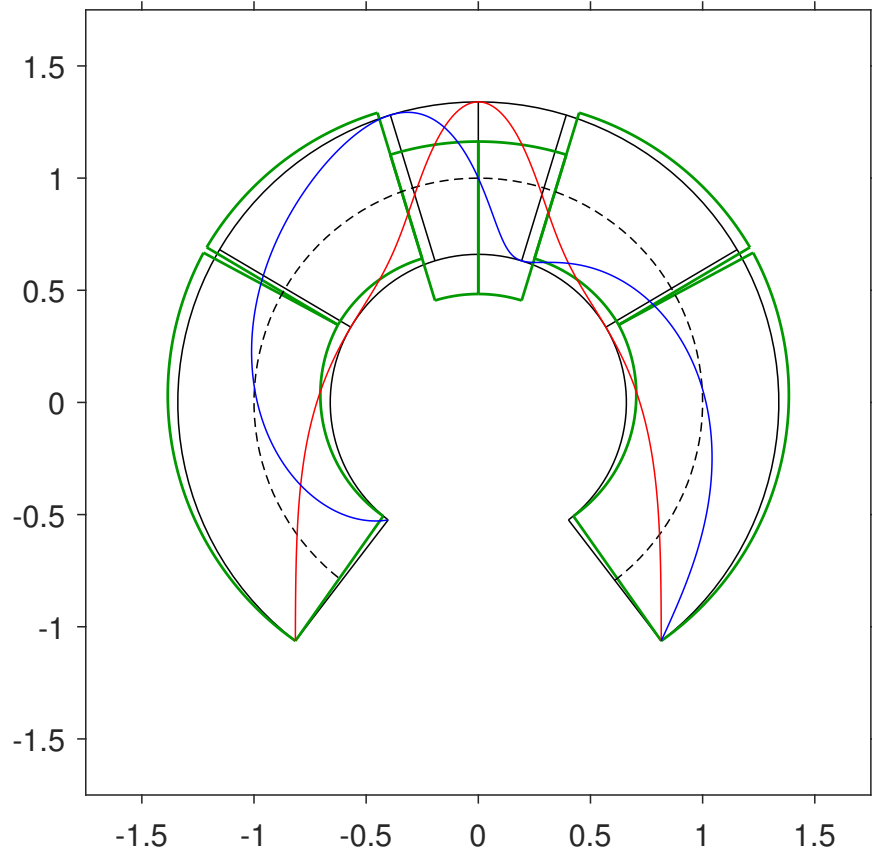


Figure 19: Least-thickness collapse mechanism, with line of thrust and line of friction: at “Triple point” with $\alpha_T = 2.487161163767182 \simeq 142.5^\circ$, $\mu_T = 1.415270827756885$ ($\varphi_T \simeq 54.8^\circ$), $\eta_T = 0.6796047320988855$: rotational-sliding (top); sliding-rotational (bottom).

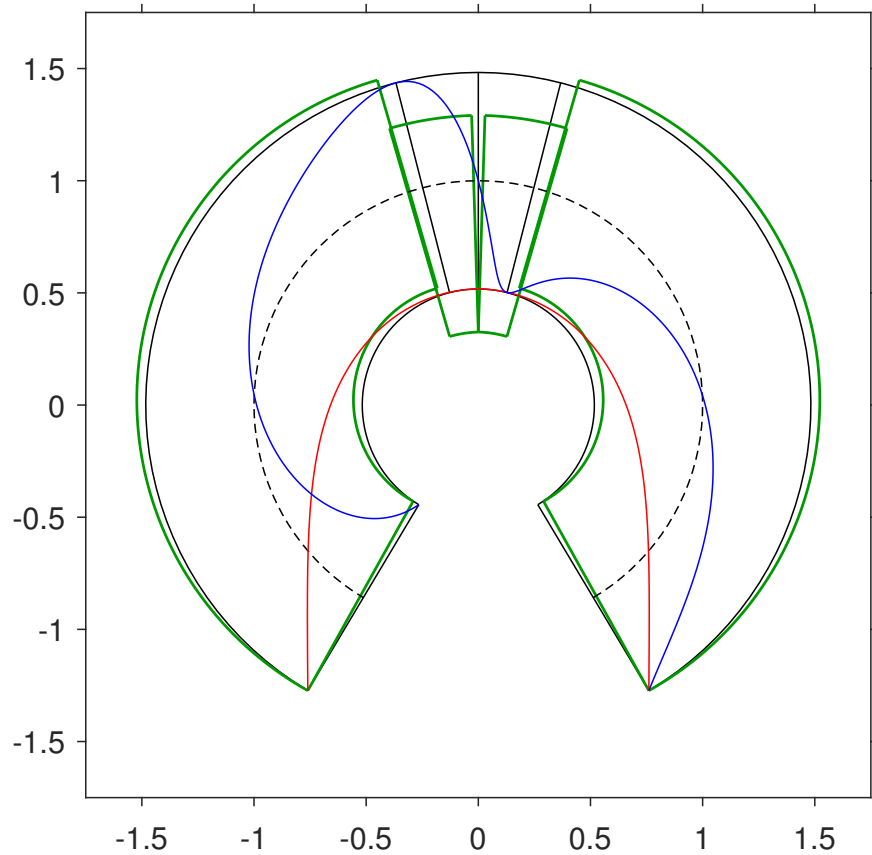
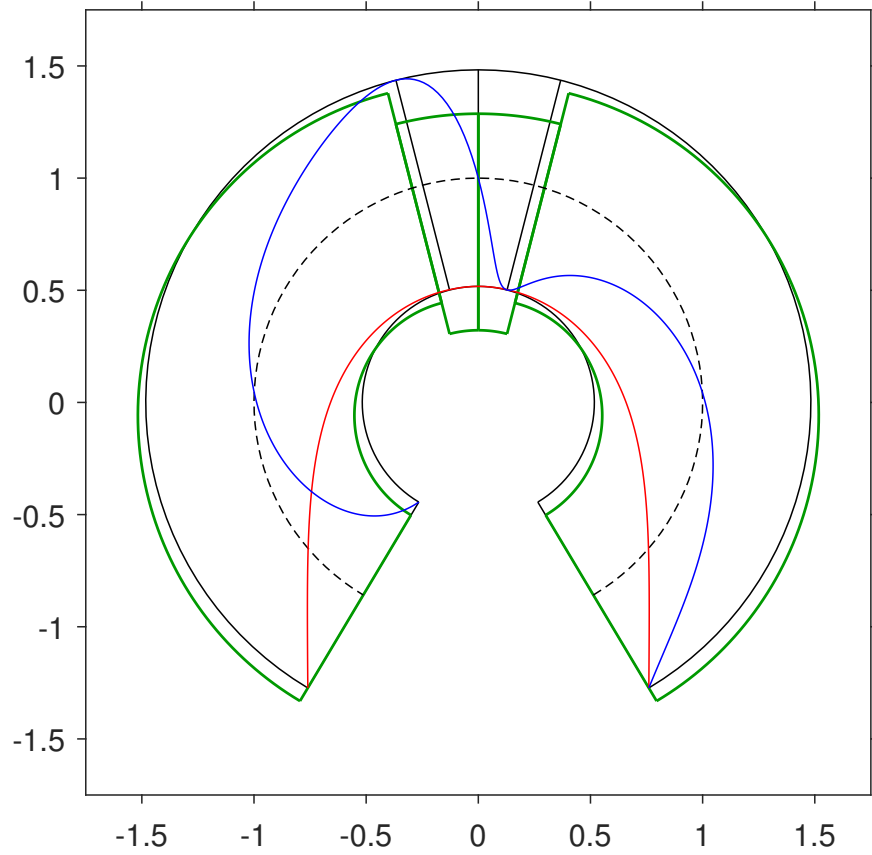


Figure 20: Least-thickness collapse mechanism, with line of thrust and line of friction: at “Junct. point” with $\alpha_J = 2.603266515104794 \simeq 149.2^\circ$, $\mu_J = 1.777213608388235$ ($\varphi_J \simeq 60.6^\circ$), $\eta_J = 0.9652414772084198$: purely-sliding (top); rotational(overturning)-sliding (low).

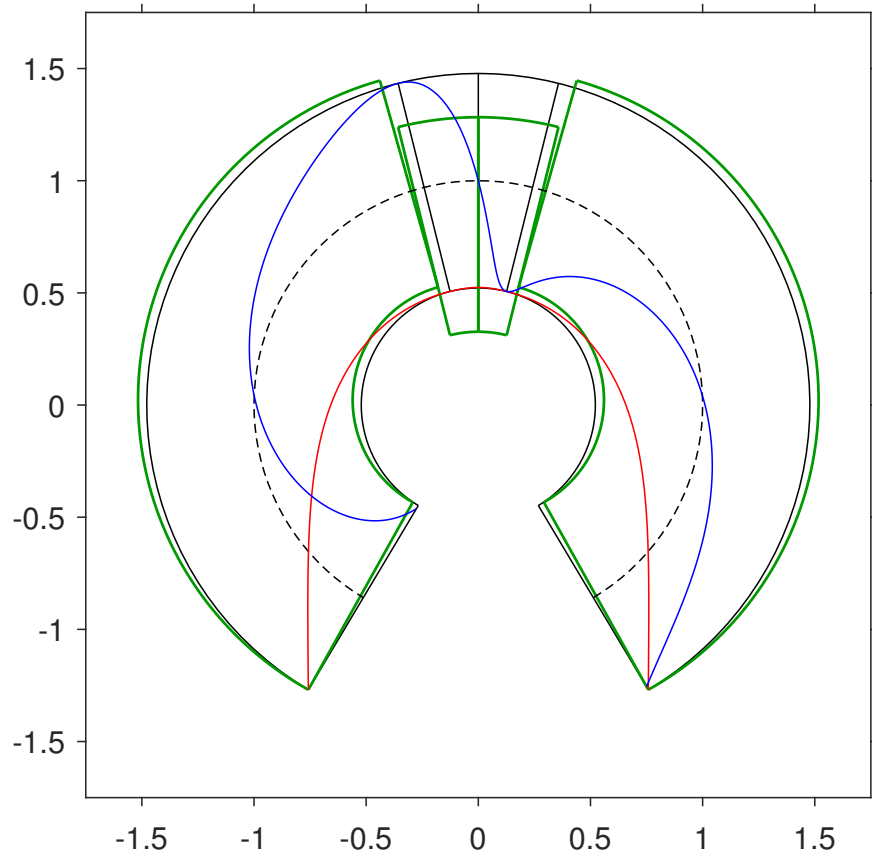
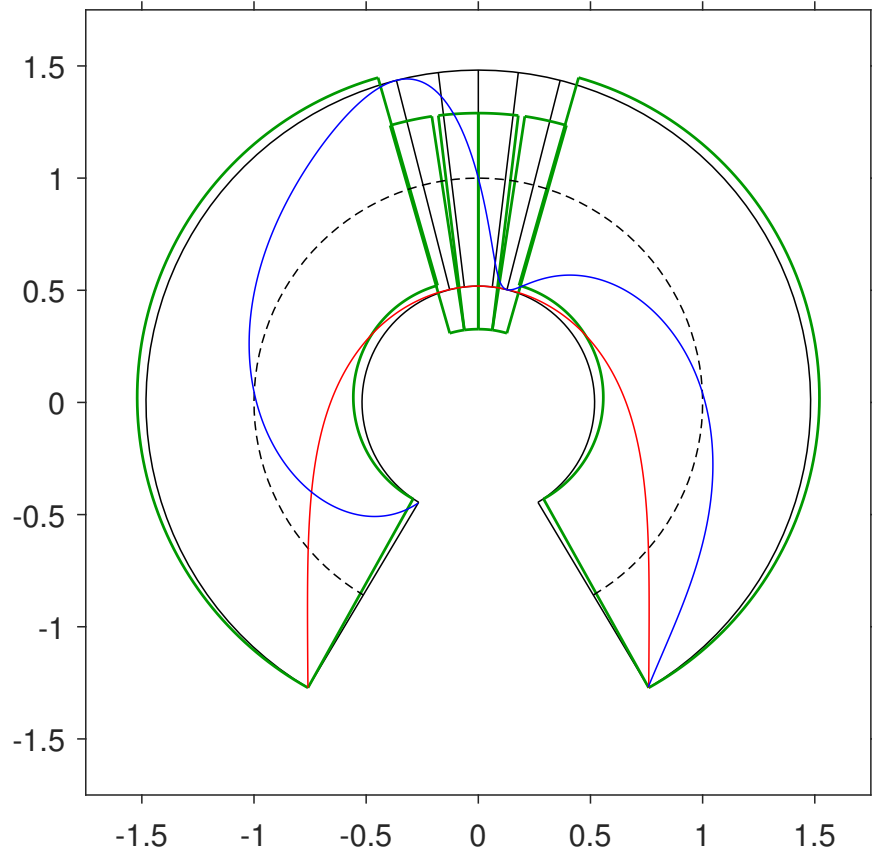


Figure 21: Least-thickness collapse mechanism, with line of thrust and line of friction: at $\alpha_J = 2.603266515104794 \simeq 149.2^\circ$ (rot.-sliding): $\mu = 1.79$ ($\varphi \simeq 60.8^\circ$), $\eta = 0.9630759684607590$ ($\beta_r < \beta_s$, top); $\mu = 1.832508693777595$ ($\varphi \simeq 61.4^\circ$), $\eta = 0.9563124518512550$ ($\beta_r = \beta_s$, low).

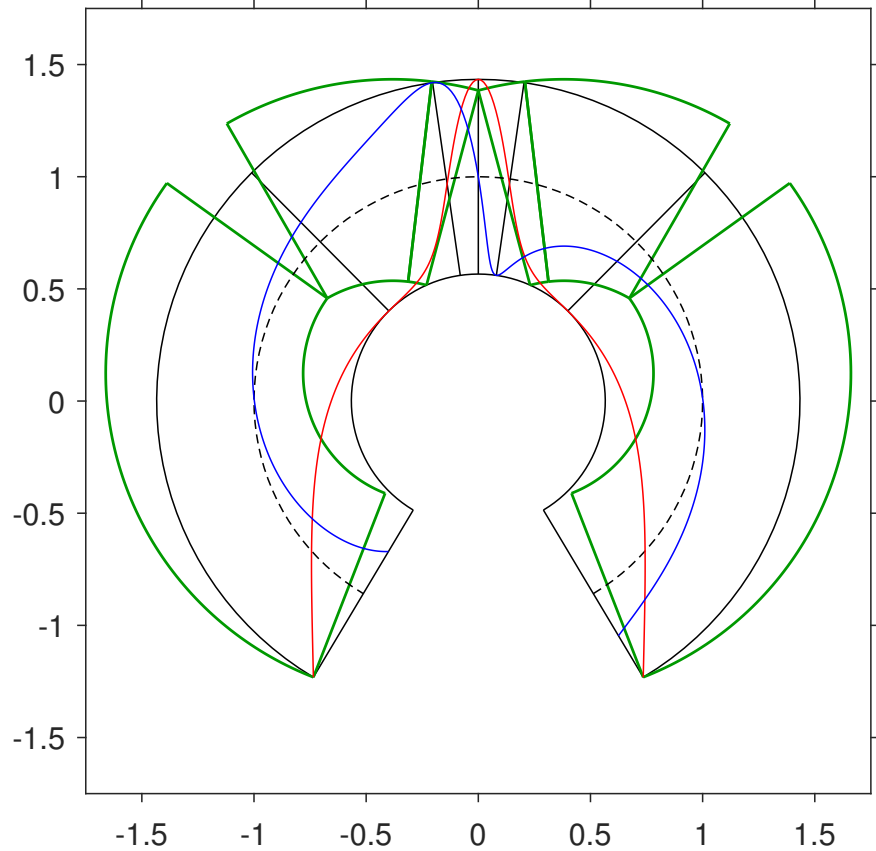
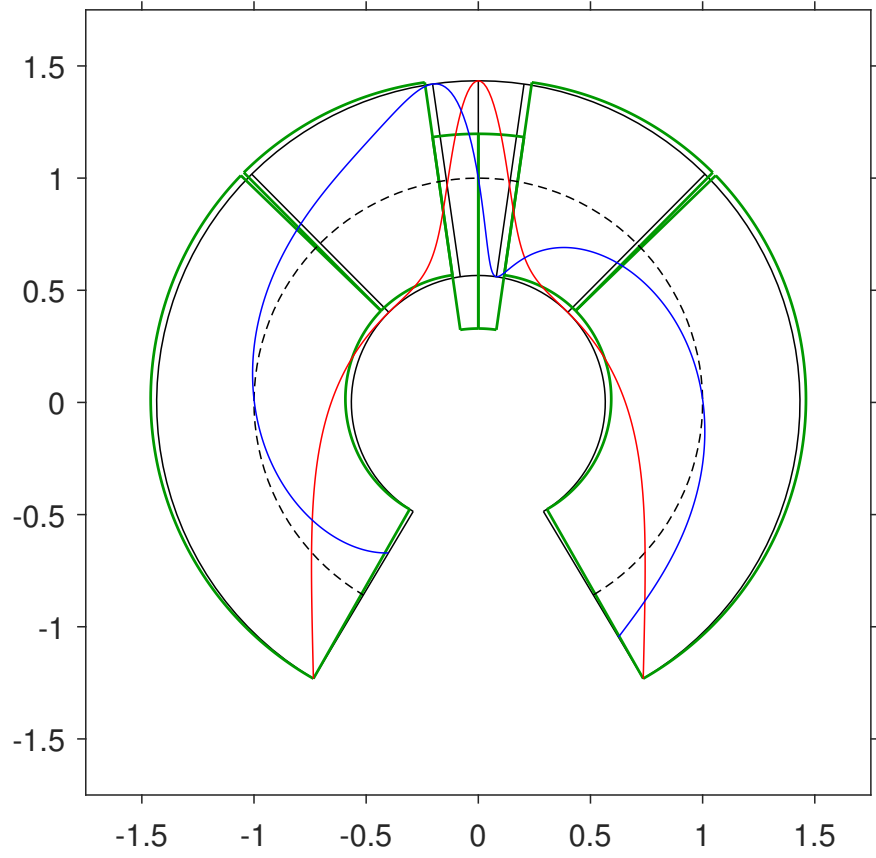


Figure 22: Least-thickness collapse mechanism, with line of thrust and line of friction: at point with $\alpha_J = 2.603266515104794 \simeq 149.2^\circ$, $\mu = 3.385846504480999$ ($\varphi \simeq 73.6^\circ$), $\eta = 0.8679273523649103$: rotational-sliding ($\beta_r > \beta_s$, top); purely-rotational (low).

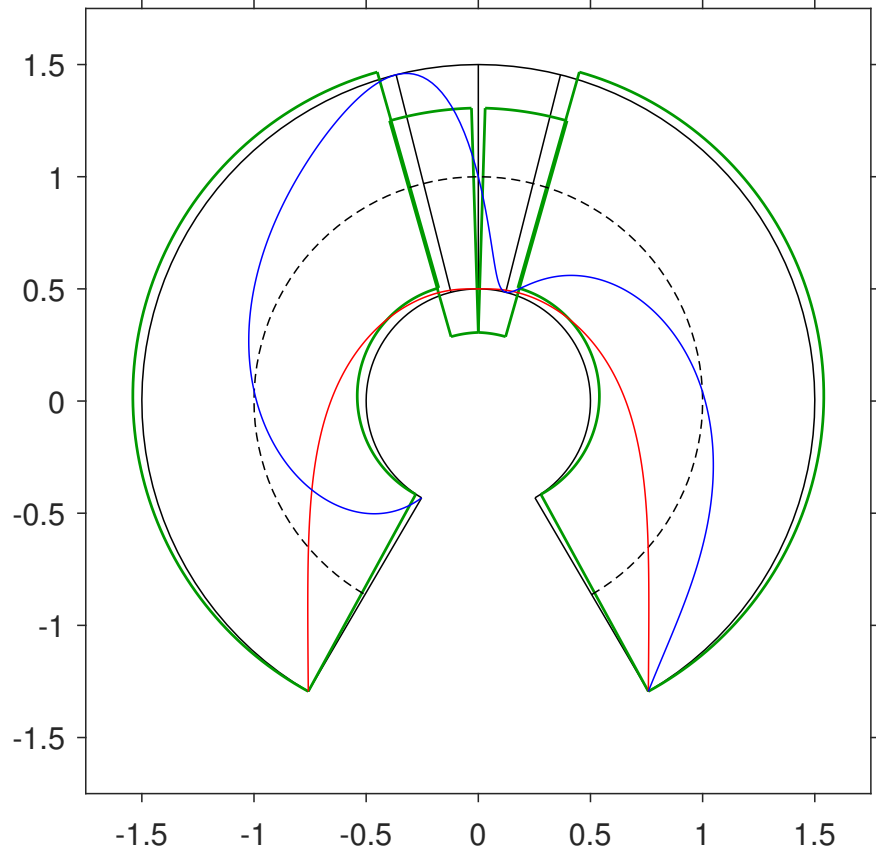
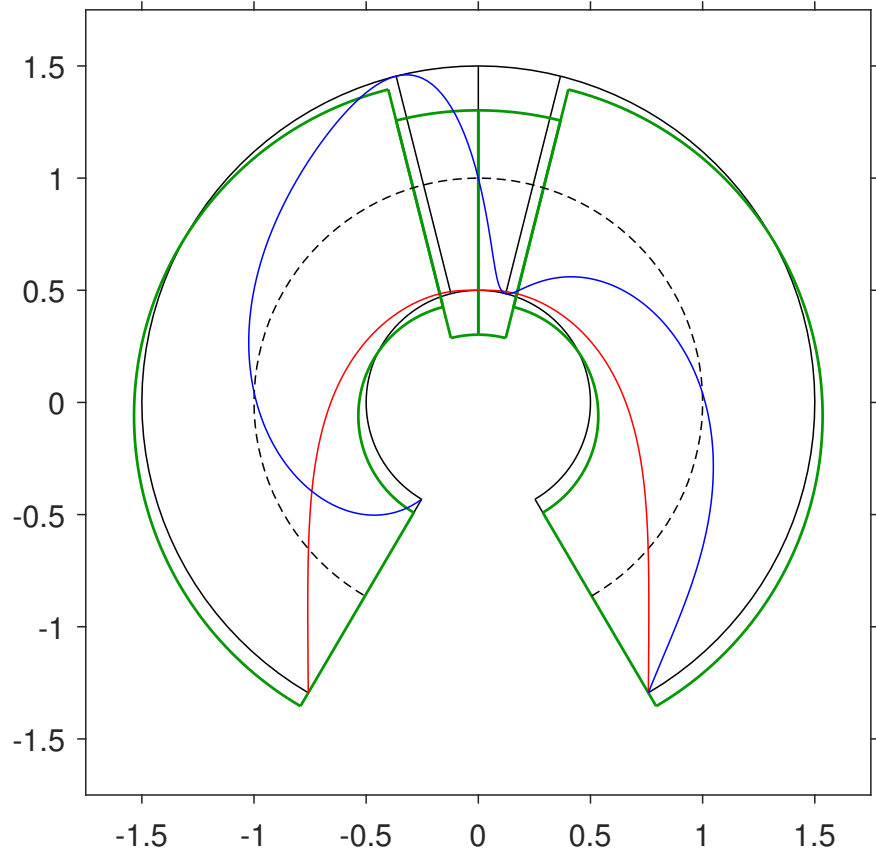


Figure 23: Least-thickness collapse mechanism, with line of thrust and line of friction: at point with $\alpha = 2.611810358168302 \simeq 149.6^\circ$, $\mu = 1.809583028035458$ ($\varphi \simeq 61.1^\circ$), $\eta = 1$: purely-sliding (top); overturning-sliding (low).

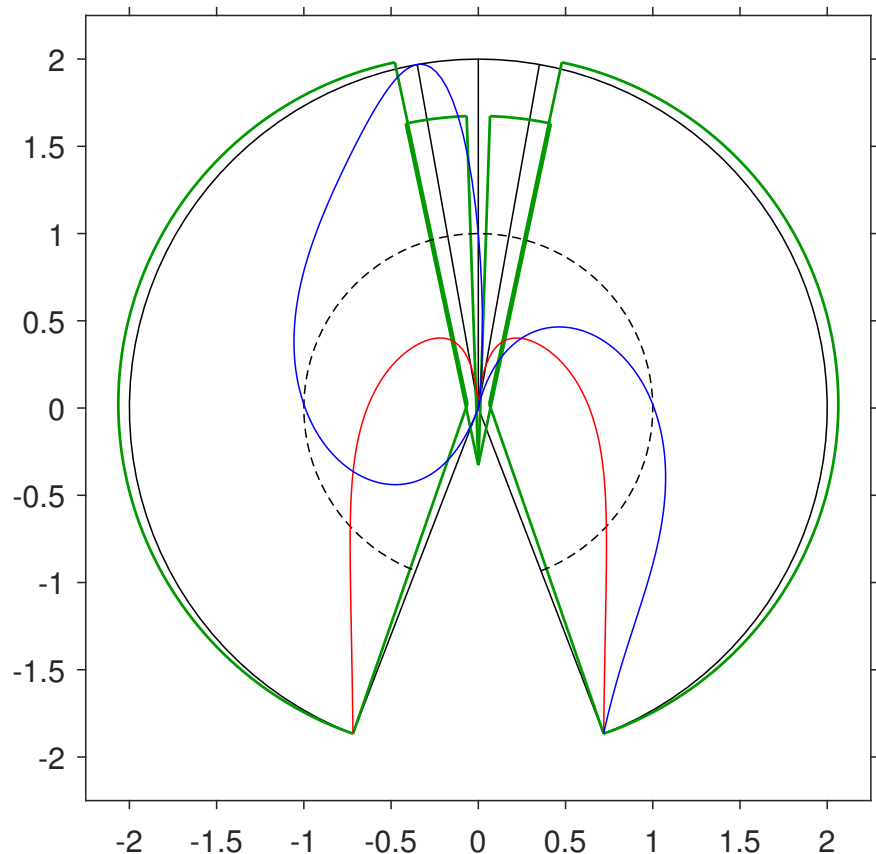
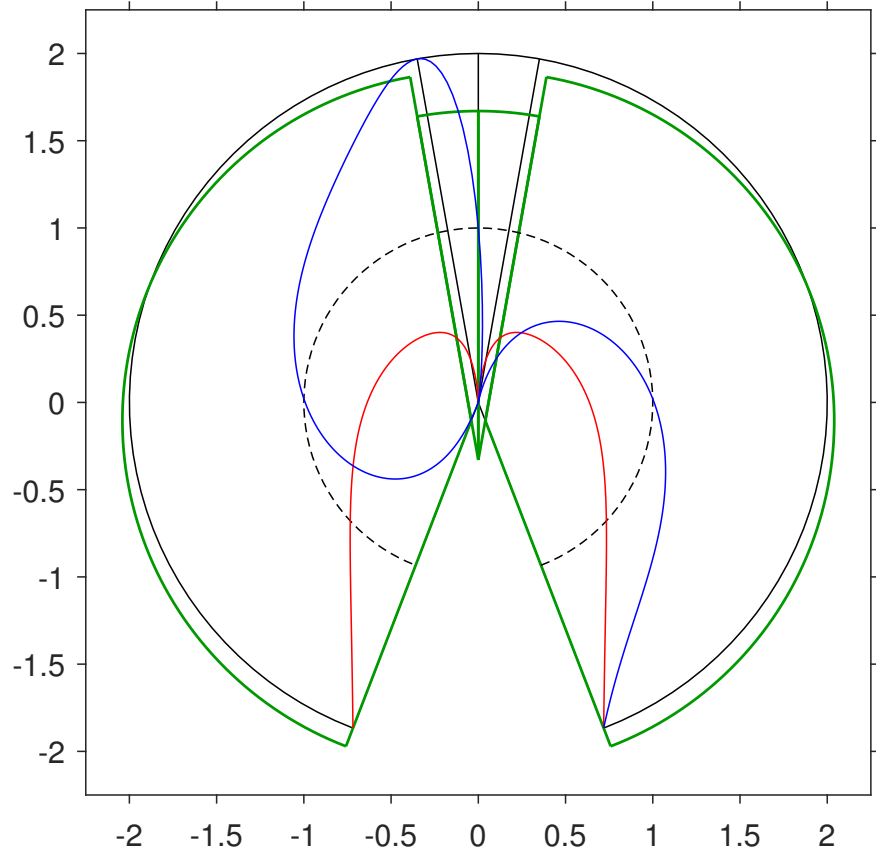


Figure 24: Least-thickness collapse mechanism, with line of thrust and line of friction: at “Border point” with $\alpha_B = 2.774176793356033 \simeq 158.9^\circ$, $\mu_B = 2.690297881776621$ ($\varphi \simeq 69.6^\circ$), $\eta_B = 2$: purely-sliding (top); overturning-sliding (low).

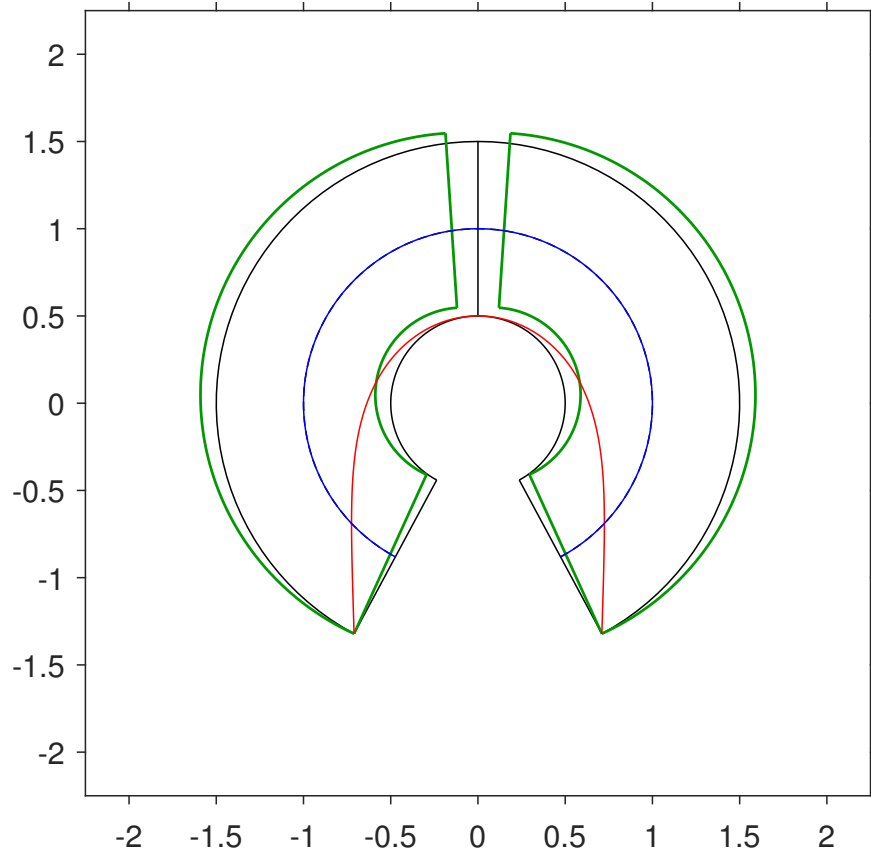
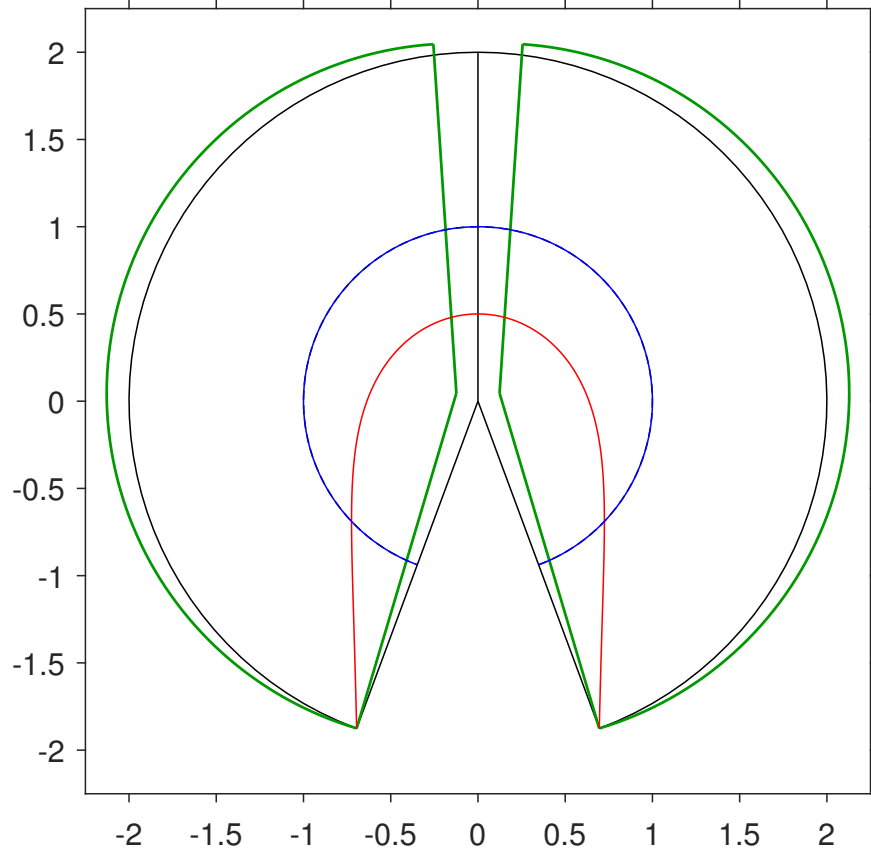


Figure 25: Least-thickness collapse mechanism, with line of thrust and line of friction: purely-overturning at $\mu \rightarrow \infty$ ($\varphi = 90^\circ$): $\alpha = 2.786498150651177 \approx 159.7^\circ$ ($A = 1/2$), $\eta = 2$ (top); $\alpha = 2.648388899151005 \approx 151.7^\circ$ ($A = 2/3$), $\eta = 1$ (low).

5 Conclusions

The present work has addressed the issue of setting the least-thickness optimization condition of self-standing symmetric circular masonry arches of general half-angle of embrace, at variable internal friction. The cardinal equilibrium and limit compatibility conditions have been outlined, in two mutually corresponding ways, and then analytically elaborated, and completely solved, in view of exploring the full range of arch behaviour in the physical space of the underlying mechanical parameters and variables.

Specifically, the safe states of the self-standing masonry arch have analytically been recovered, and the domains of arch collapse located, with the contour boundaries separating them and the localization of all the relevant collapse mechanisms, possibly including sliding, as linked to the presence of finite friction.

At given specific self-weight, herein with classical Heyman-like uniform distribution along geometrical centreline (a separate derivation for true Milankovitch-like uniform self-weight distribution may subsequently be derived, as a generalization of the present analysis), radius and out-of-plane depth of the symmetric circular masonry arch, the least-thickness self-standing condition of minimum thickness-to-radius ratio is sought, as an iconic structural form-optimization problem, at variable physical parameters, which are the half-opening angle and the underlying friction coefficient (angle) at the theoretical (radial) joints of the continuous arch. This sets, in principle, a rather simple, and fascinating, mechanical system. Once all characteristic solutions are investigated, and delivered, with no a priori limitations on the ideally legitimate underlying mechanical parameters (for instance, thickness-to-radius ratio between 0 and 2, half-opening angle among 0 and π , friction coefficient from 0 to ∞), rather surprising, variegated and intricate features arise, in terms of resulting outcomes and recorded richness of manifestations, in both academic and engineering terms, for the formulated mechanical problem.

The above has been revealed thanks to a complete and systematic analytical approach, up to deliver “exact” solutions for the problem at hand, and then further illustrated and validated by a separate numerical treatment based on a home-made Complementarity Problem/Mathematical Programming formulation and implementation. While the former is necessarily linked and likely limited to the intrinsic simplicity of the morphological shape and assumed self-weight loading condition of the circular masonry arch, still allowing to recover “exact” solutions, with such rich features, the latter, with consistent geometrical adaptations, may then allow for further inspections and applications to other reference configurations of the masonry arch, in view of generalizing the present results to other arch settings, where a complete analytical treatment may become unfeasible, and also in view of the analysis of specific practical cases, with given chunk geometries and external characteristics.

This may lead to further possible developments of the present research investigation, enquiring, for instance, unsymmetric or different geometrical shapes of the masonry arch [23, 26, 31–34, 42–44, 47, 49, 61, 62], issues of stereotomy (i.e. the shape of the stone cuttings of the mutual joints of voussoir arches [9, 29, 38–41, 45]), effects of boundary conditions [22, 35–37], different loading conditions (e.g. including lateral actions [22, 25, 27, 33, 61, 62]), and so on.

However, the considered neat setting of a symmetric circular masonry arch under self-weight shall constitute a main, fundamental reference, once now fully resolved in characteristic features, even at variable finite internal friction, toward a general perception and understanding of the Mechanics of masonry arches.

Acknowledgments

This work has been developed at the University of Bergamo, School of Engineering (Dalmine). The support by ministerial (MUR) funding “Fondi di Ricerca d’Ateneo ex 60%” at the University of Bergamo is gratefully acknowledged.

Compliance with Ethical Standards

The authors declare that they have no conflict of interest.

References

- [1] Milankovitch, M. (1904). Beitrag zur Theorie der Druckkurven. Dissertation zur Erlangung der Doctorwürde, K.K. Technische Hochschule, Wien.
- [2] Milankovitch, M. (1907). Theorie der Druckkurven, Zeitschrift für Mathematik und Physik, 55, pp. 1-27.
- [3] Foce, F. (2007). Milankovitch’s Theorie der Druckkurven: Good mechanics for masonry architecture, Nexus Network Journal, 9(2), pp. 185-210. DOI: 10.1007/s00004-007-0039-9.
- [4] Heyman, J. (1966). The stone skeleton, International Journal of Solids and Structures, 2(2), pp. 249-279. DOI: 10.1016/0020-7683(66)90018-7.
- [5] Heyman, J. (1967). On shell solutions for masonry domes, International Journal of Solids and Structures, 3(2), pp. 227-241. DOI: 10.1016/0020-7683(67)90072-8.
- [6] Heyman, J. (1969). The safety of masonry arches, International Journal of Mechanical Sciences, 11(4), pp. 363-385. DOI: 10.1016/0020-7403(69)90070-8.
- [7] Heyman, J. (1977). Equilibrium of Shell Structures, Clarendon Press, Oxford.
- [8] Heyman, J. (1982). The Masonry Arch, Ellis Horwood Ltd., Chichester.
- [9] Heyman, J. (2009). La coupe des pierres, In: Proceedings of the Third International Congress on Construction History, Brandenburg University of Technology, Cottbus, Germany, 20-24 May 2009, 2, pp. 807-812.
- [10] Cocchetti, G., Colasante, G., Rizzi, E. (2011). On the analysis of minimum thickness in circular masonry arches. Part I: State of the art and Heyman’s solution. Part II: Present CCR solution. Part III: Milankovitch-type solution, Applied Mechanics Reviews, ASME, September 01, 2011, 64(5), Paper 050802 (Oct. 01, 2012), pp. 1-27. DOI: 10.1115/1.4007417.
- [11] Rizzi, E., Rusconi, F., Cocchetti, G. (2014). Analytical and numerical DDA analysis on the collapse mode of circular masonry arches, Engineering Structures, 60(February 2014), pp. 241-257. DOI: 10.1016/j.engstruct.2013.12.023.
- [12] Cocchetti, G., Rizzi, E. (2020). Analytical and numerical analysis on the collapse modes of least-thickness circular masonry arches at decreasing friction, Frattura ed Integrità Strutturale - Fracture and Structural Integrity, Special Issue on: Fracture and

Damage Detection in Masonry Structures, 14(51), pp. 356-375, available Open Access at <https://www.fracturae.com/index.php/fis/article/view/2554>. DOI: 10.3221/IGF-ESIS.51.26.

- [13] Cocchetti, G., Rizzi, E. (2020). Non-linear programming numerical formulation to acquire limit self-standing conditions of circular masonry arches accounting for limited friction, International Journal of Masonry Research and Innovation, Special Issue on: 10IMC Masonry Research in the Third Millennium From Theory to Practical Applications, 5(4), pp. 569-617. DOI: 10.1504/IJMRI.2020.111806.
- [14] Cocchetti, G., Rizzi, E. (2020). Static upper/lower thrust and kinematic work balance stationarity for least-thickness circular masonry arch optimization, Journal of Optimization Theory and Applications, Special Issue on: Computational Optimization for Structural Engineering and Applications, 187(3), pp. 707-757, available Open Access at <https://link.springer.com/article/10.1007/s10957-020-01772-0>. DOI: 10.1007/s10957-020-01772-0.
- [15] Cocchetti, G., Rizzi, E. (2021). Least-thickness symmetric circular masonry arch of maximum horizontal thrust, Archive of Applied Mechanics, 91(6), pp. 2617-2639, available Open Access at <https://link.springer.com/article/10.1007/s00419-021-01909-1>. DOI: 10.1007/s00419-021-01909-1.
- [16] Como, M. (1992). Equilibrium and collapse of masonry bodies, Meccanica, 27(3), pp. 185-194. DOI: 10.1007/BF00430044.
- [17] Blasi, C., Foraboschi, P. (1994). Analytical approach to collapse mechanisms of circular masonry arch, Journal of Structural Engineering, ASCE, 120(8), pp. 2288-2309. DOI: 10.1061/(ASCE)0733-9445(1994)120:8(2288).
- [18] Boothby, T.E. (1996). Analytical approach to collapse mechanisms of circular masonry arch. Discussion on the paper by Blasi and Foraboschi (1994), with Closure by P. Foraboschi and C. Blasi, J. of Structural Engineering, ASCE, 122(8), pp. 978-980. DOI: 10.1061/(ASCE)0733-9445(1996)122:8(978).
- [19] Lucchesi, M., Padovani, C., Pasquinelli, G., Zani, N. (1997). On the collapse of masonry arches, Meccanica, 32(4), pp. 327-346. DOI: 10.1023/A:1004275223879.
- [20] Sinopoli, A., Corradi, M., Foce, F. (1997). Modern formulation for preelastic theories on masonry arches, Journal of Engineering Mechanics, ASCE, 123(3), pp. 204-213. DOI: 10.1061/(ASCE)0733-9399(1997)123:3(204).
- [21] Ochsendorf, J.A. (2002). Collapse of Masonry Structures, Doctoral Dissertation, University of Cambridge, UK. DOI: 10.17863/CAM.14048.
- [22] Ochsendorf, J.A. (2006). The masonry arch on spreading supports, The Structural Engineer, 84(2), pp. 29-36.
- [23] Romano, A., Ochsendorf, J.A. (2009). The mechanics of Gothic masonry arches, International Journal of Architectural Heritage, 4(1), pp. 59-82. DOI: 10.1080/15583050902914660.

- [24] Gago, A.S. (2004). Análise Estrutural de Arcos, Abóbadas e Cúpulas - Contributo para o Estudo do Património Construído, Dissertação, Doutoramento em Engenharia Civil, Orientador: Lamas A., Universidade Técnica de Lisboa, Instituto Superior Técnico, IST-UTL, Dezembro de 2004.
- [25] Gago, A.S., Alfaiate, J., Lamas, A. (2011). The effect of the infill in arched structures: Analytical and numerical modelling, *Engineering Structures*, 33(5), pp. 1450-1458. DOI: 10.1016/j.engstruct.2010.12.037.
- [26] Alexakis, H., Makris, N. (2013). Minimum thickness of elliptical masonry arches, *Acta Mechanica*, 224(12), pp. 2977-2991. DOI: 10.1007/s00707-013-0906-2.
- [27] Alexakis, H., Makris, N. (2014). Limit equilibrium analysis and the minimum thickness of circular masonry arches to withstand lateral inertial loading, *Archive of Applied Mechanics*, 84(5), pp. 757-772. DOI: 10.1007/s00419-014-0831-4.
- [28] Alexakis, H., Makris, N. (2015). Limit equilibrium analysis of masonry arches, *Archive of Applied Mechanics*, 85(9-10), pp. 1363-1381. DOI: 10.1007/s00419-014-0963-6.
- [29] Makris, N., Alexakis, H. (2013). The effect of stereotomy on the shape of the thrust-line and the minimum thickness of semicircular masonry arches, *Archive of Applied Mechanics*, 83(10), pp. 1511-1533. DOI: 10.1007/s00419-013-0763-4.
- [30] Bagi, K. (2014). When Heyman's Safe Theorem of rigid block systems fails: Non-Heymanian collapse modes of masonry structures, *International Journal of Solids and Structures*, 51(14), pp. 2696-2705. DOI: 10.1016/j.ijsolstr.2014.03.041
- [31] Simon, J., Bagi, K. (2016). Discrete element analysis of the minimum thickness of oval masonry domes, *International Journal of Architectural Heritage*, 10(4), pp. 457-475. DOI: 10.1080/15583058.2014.996921.
- [32] Lengyel, G. (2018). Minimum thickness of the gothic arch, *Archive of Applied Mechanics*, 88(5), pp. 769-788. DOI: 10.1007/s00419-018-1341-6.
- [33] Cavalagli, N., Gusella, V., Severini, L. (2016). Lateral loads carrying capacity and minimum thickness of circular and pointed masonry arches, *International Journal of Mechanical Sciences*, 115-116(September 2016), pp. 645-656. DOI: 10.1016/j.ijmecsci.2016.07.015.
- [34] Cavalagli, N., Gusella, V., Severini, L. (2017). The safety of masonry arches with uncertain geometry, *Computers and Structures*, 188(August 2017), pp. 17-31. DOI: 10.1016/j.compstruc.2017.04.003.
- [35] Zampieri, P., Cavalagli, N., Gusella, V., Pellegrino, C. (2018). Collapse displacements of masonry arch with geometrical uncertainties on spreading supports, *Computers and Structures*, 208(1 October 2018), pp. 118-129. DOI: 10.1016/j.compstruc.2018.07.001.
- [36] Zampieri, P., Faleschini, F., Zanini, M.A., Simoncello, N. (2018). Collapse mechanisms of masonry arches with settled springing, *Engineering Structures*, 156(1 February 2018), pp. 363-374. DOI: 10.1016/j.engstruct.2017.11.048.

- [37] Galassi, S., Misseri, G., Rovero, L., Tempesta, G. (2018). Failure modes prediction of masonry voussoir arches on moving supports, *Engineering Structures*, 173(15 October 2018), pp. 706-717. DOI: 10.1016/j.engstruct.2018.07.015.
- [38] Gáspár, O., Sipos, A.A., Sajtos, I. (2018). Effect of stereotomy on the lower bound value of minimum thickness of semi-circular masonry arches, *International Journal of Architectural Heritage*, 12(6), pp. 899-921. DOI: 10.1080/15583058.2017.1422572.
- [39] Gáspár, O., Sajtos, I., Sipos, A.A. (2021). Friction as a geometric constraint on stereotomy in the minimum thickness analysis of circular and elliptical masonry arches, *International Journal of Solids and Structures*, 225(15 August 2021), 111056, pp. 1-18. DOI: 10.1016/j.ijsolstr.2021.111056.
- [40] Gáspár, O., Sajtos, I., Sipos, A.A. (2022). Multi-hinge failure mechanisms of masonry arches subject to self-weight as derived from minimum thickness analysis, *International Journal of Architectural Heritage*, Published online 28 June 2022, pp. 1-29. DOI: 10.1080/15583058.2022.2084702.
- [41] Sipos, A.A. (2023). About the number of hinges at failure of semicircular and pointed masonry arches, *Mathematics and Mechanics of Solids*, OnlineFirst September 30, 2023, pp. 1-11. DOI: 10.1177/10812865231196796.
- [42] Aita, D., Barsotti, R., Bennati, S. (2019). Looking at the collapse modes of circular and pointed masonry arches through the lens of Durand-Claye's stability area method, *Archive of Applied Mechanics*, 89(8), pp. 1537-1554. DOI: 10.1007/s00419-019-01526-z.
- [43] Aita, D., Sinopoli, A. (2020). Revisiting Monasterio's unpublished manuscript: a critical review of the collapse modes analysis of non-symmetric and symmetric masonry arches, *International Journal of Architectural Heritage*, 14(5), pp. 762-793. DOI: 10.1080/15583058.2019.1648586.
- [44] Aita, D., Sinopoli, A. (2021). Two different approaches for collapse of nonsymmetric masonry arches: Monasterio's treatment versus limit equilibrium analysis, *Journal of Engineering Mechanics (ASCE)*, 147(10), 04021071, pp. 1-18. DOI: 10.1061/(ASCE)EM.1943-7889.0001989.
- [45] Aita, D. (2022). Between stereotomy and mechanics: joints inclination and minimum thickness in frictionless pointed and circular arches, *International Journal of Masonry Research and Innovation*, 7(1-2), pp. 61-88. DOI: 10.1504/IJMRI.2022.119867.
- [46] Block, P., DeJong, M., Ochsendorf, J. (2006). As hangs the flexible line: equilibrium of masonry arches, *Nexus Network Journal*, 8(2), pp. 13-24. DOI: 10.1007/s00004-006-0015-9.
- [47] Nikolić, D. (2017). Thrust line analysis and the minimum thickness of pointed masonry arches, *Acta Mechanica*, 228(6), pp. 2219-2236. DOI: 10.1007/s00707-017-1823-6.
- [48] Nikolić, D. (2019). Catenary arch of finite thickness as the optimal arch shape. *Structural and Multidisciplinary Optimization*, 60(5), pp. 1957-1966. DOI: 10.1007/s00158-019-02304-9.

- [49] Nikolić, D. (2020). Thrust line analysis of triangular arches, *Archive of Applied Mechanics*, 90(9), pp. 1861-1874. DOI: 10.1007/s00419-020-01701-7.
- [50] Nikolić, D. (2022). A note on the catenary arch bending-moment-free paradox, *Meccanica*, 57(6), pp. 1457-1462. DOI: 10.1007/s11012-022-01513-9.
- [51] Ricci, E., Fraddosio, A., Piccioni, M.D., Sacco, E. (2019). A new numerical approach for determining optimal thrust curves of masonry arches, *European Journal of Mechanics - A/Solids*, 75(May-June 2019), pp. 426-442. DOI: 10.1016/j.euromechsol.2019.02.003.
- [52] Tempesta, G., Galassi, S. (2019). Safety evaluation of masonry arches. A numerical procedure based on the thrust line closest to the geometrical axis, *International Journal of Mechanical Sciences*, 155(May 2019), pp. 206-221. DOI: 10.1016/j.ijmecsci.2019.02.036.
- [53] Nodargi, N.A., Bisegna, P. (2020). Thrust line analysis revisited and applied to optimization of masonry arches, *International Journal of Mechanical Sciences*, 179(1 August 2020), Article number 105690179, pp. 1-13. DOI: 10.1016/j.ijmecsci.2020.105690.
- [54] Boothby, T.E. (1994). Stability of masonry piers and arches including sliding, *Journal of Engineering Mechanics*, 120(2), pp. 304-319. DOI: 10.1061/(ASCE)0733-9399(1994)120:2(304).
- [55] Sinopoli, A., Rapallini, M., Smars, P. (2004). Plasticity, Coulomb friction and sliding in the limit analysis of masonry arches, Proc. of 4th Int. Conference on Arch Bridges (ARCH'04), Barcelona, 17-19 November 2004, P. Roca and E. Oñate (Eds.), CIMNE, pp. 1-10.
- [56] Sinopoli, A., Aita, D., Foce, F. (2007). Further remarks on the collapse mode of masonry arches with Coulomb friction, Proc. of 5th Int. Conference on Arch Bridges (ARCH'07), Funchal, Madeira, Portugal, September 12-14, 2007, P.B. Lourenço, D.B. Oliveira, A. Portela (Eds.), Multicomp, Lda Publishers, Madeira, pp. 649-657.
- [57] Smars, P. (2000). Etudes sur la stabilité des arcs et voûtes: Confrontation des méthodes de l'analyse limite aux voûtes gothique en Brabant, Doctoral Thesis, Katholieke Universiteit Leuven, Belgium, 229 pages.
- [58] Smars, P. (2008). Influence of friction and tensile resistance on the stability of masonry arches, Structural Analysis of Historic Construction: Preserving Safety and Significance - Proceedings of the 6th International Conference on Structural Analysis of Historic Construction (SAHC 2008), D'Ayala D. and Fodde E. Eds., Bath (UK), Volume 2, pp. 1199-1206, Taylor & Francis Group, London, 2-4 July 2008. ISBN: 0415468728; 978-041546872-5.
- [59] Smars, P. (2010). Kinematic stability of masonry arches, *Advanced Materials Research*, 133-134, pp. 429-434. DOI: 10.4028/www.scientific.net/AMR.133-134.429.
- [60] Baggio, C., Trovalusci, P. (2000). Collapse behaviour of three-dimensional brick-block systems using non-linear programming, *Structural Engineering and Mechanics*, 10(2), pp. 181-195. DOI: 10.12989/sem.2000.10.2.181.
- [61] Rios, A.J., Nela, B., Pingaro, M., Reccia, E., Trovalusci, P. (2022). Rotation and sliding collapse mechanisms for in plane masonry pointed arches: statistical

- parametric assessment, *Engineering Structures*, 262(1 July 2022), 114338, pp. 1-16. DOI: 10.1016/j.engstruct.2022.114338.
- [62] Rios, A.J., Nela, B., Pingaro, M., Reccia, E., Trovalusci, P. (2023). Parametric analysis of masonry arches following a limit analysis approach: Influence of joint friction, pier texture, and arch shallowness, *Mathematics and Mechanics of Solids*, OnlineFirst July 11, 2023, pp. 1-29. DOI: 10.1177/10812865231175385.
- [63] Casapulla, C., Lauro, F. (2000). A simple computation tool for the limit-state analysis of masonry arches, Proc. of 5th Int. Congress on Restoration of Architectural Heritage, Università di Firenze, 17-24 September 2000, CDROM Proc., pp. 2056-2064, 9 pages.
- [64] Gilbert, M., Casapulla, C., Ahmed, H. M. (2006). Limit analysis of masonry block structures with non-associative frictional joints using linear programming, *Computers and Structures*, 84(13-14), pp. 873-887. DOI: 10.1016/j.compstruc.2006.02.005.
- [65] D'Ayala, D., Tomasoni, E. (2011). Three-dimensional analysis of masonry vaults using limit state analysis with finite friction, *International Journal of Architectural Heritage*, 5(2), pp. 140-171. DOI: 10.1080/15583050903367595.
- [66] Olivito, R.S., Esposito, M., Totaro, N. (2016). Experimental investigation for the friction evaluation in the masonry structures, *International Journal of Masonry Research and Innovation*, 1(1), pp. 22-47. DOI: 10.1504/IJMRI.2016.074729.
- [67] Trentadue, F., Quaranta, G. (2013). Limit analysis of frictional block assemblies by means of fictitious associative-type contact interface laws, *International Journal of Mechanical Sciences*, 70 (May 2013), pp. 140-145. DOI: 10.1016/j.ijmecsci.2013.02.012.
- [68] Trentadue, F., De Tommasi, D., Marasciuolo, N., Vitucci, G. (2024). Thrust in a symmetric masonry arch with frictional joints on spreading supports, *Acta Mechanica*, 235(2), pp. 659-670. DOI: 10.1007/s00707-023-03759-0.
- [69] Hua, Y., Milani, G. (2022). Rigid Block Limit Analysis of Masonry Arches with Associated and Non-associated Slides, in: G. Milani and V. Sarhosis (Eds.), *From Corbel Arches to Double Curvature Vaults*, Springer Nature Switzerland AG, pp. 169-203. DOI: 10.1007/978-3-031-12873-8_7.